Multiscale discontinuous Galerkin methods and applications

by

Wei Wang

B.Sc., University of Science and Technology of China, P.R.China, 2004

M.Sc., Brown University, RI, 2006

A dissertation submitted in partial fulfillment of the
requirements for the degree of Doctor of Philosophy
in the Division of Applied Mathematics at Brown University

PROVIDENCE, RHODE ISLAND

May 2008

Abstract of "Multiscale discontinuous Galerkin methods and applications" by Wei Wang, Ph.D., Brown University, May 2008

This thesis contains three related topics on the multiscale discontinuous Galerkin (DG) methods and applications.

In the first part, we present a multiscale model for numerical simulation of dynamics of crystalline solids. The method couples nonlinear elastodynamics as the continuum description and molecular dynamics as another component at the atomic scale. The governing equations on the macroscale are solved by the DG method, which is built up with an appropriate local curl-free space to produce a coherent displacement field.

In the second part, we develop a multiscale local discontinuous Galerkin (LDG) method to simulate the 1-D stationary Schrödinger-Poisson problem. The WKB-LDG method is proposed for solving the Schrödinger equation and provides a significant reduction of both the computational cost and memory. It has the advantages of the DG methods including their flexibility in h-p adaptivity and the allowance of complete discontinuity at element interfaces compared with a traditional continuous finite element Galerkin methodology.

In the third part, we develop a multiscale DG method for solving a class of second order elliptic problems with rough coefficients based on the previous work of Yuan and Shu [75]. The main ingredient of this method is to use a non-polynomial multiscale approximation space in the DG method to capture the solutions without resolving the fine-scale structure of the solution. We generalize the analysis of the multiscale Babuška-Zlámal DG method to the case of $u \in H^1([0,1])$. We also propose a multiscale local discontinuous Petrov-Galerkin method and a multiscale interior penalty DG method in the numerical tests.

This dissertation by Wei Wang is accepted in its present form
by the Division of Applied Mathematics as satisfying the
dissertation requirement for the degree of Doctor of Philosophy.

Date_____ _____

Chi-Wang Shu, Ph.D., Advisor

Recommended to the Graduate Council

Date_____ _____

David Gottlieb, Ph.D., Reader

Date_____ _____

Jan S. Hesthaven, Ph.D., Reader

Approved by the Graduate Council

Date_____ _____

Sheila Bonde, Dean of the Graduate School

The Vita of Wei Wang

Born on Feburary 2, 1982 in Heilongjiang, China.

Education

- M.Sc. in Applied Mathematics, Brown University, May 2006.
- B.Sc. in Mathematics, University of Science and Technology of China, P.R. China, June 2004.

Publications/Preprints

- W. Wang, X. Li and C.-W. Shu, *The discontinuous Galerkin method for the multiscale modeling of dynamics of crystalline solids*, Multiscale Modeling and Simulation: A SIAM Interdisciplinary Journal, to appear.
- W. Wang and C.-W. Shu, *The WKB local discontinuous Galerkin method for the simulation of Schrodinger equation in a resonant tunneling diode*, Journal of Scientific Computing, submitted.

Research Interests

- High order numerical methods for conservation laws, especially discontinuous Galerkin method, weighted ENO method and spectral methods.
- Multiscale discontinuous Galerkin methods for solid mechanics.
- Multiscale discontinuous Galerkin methods for semiconductor device simulation.
- discontinuous Galerkin methods with non-polynomial building blocks.

Academic Experience

- Research Assistant: Division of Applied Mathematics, Brown University, Spring 2008.
- Teaching Assistant: *Operations Research*, Division of Applied Mathematics, Brown University, Fall 2007.
- Research Assistant: Division of Applied Mathematics, Brown University, June 2006 – August 2007.
- Teaching Assistant: *Methods of Applied Mathematics II*, Division of Applied Mathematics, Brown University, Spring 2006.
- Teaching Assistant: *Methods of Applied Mathematics I*, Division of Applied Mathematics, Brown University, Fall 2005.

Awards and Honors

- The Stella Dafermos Award, 2008, Division of Applied Mathematics, Brown University.
- Graduate Student Fellowship, 2004-2005, Brown University.
- Zhang Zongzhi Fellowship, Outstanding Students Scholarship, 2000-2003, University of Science and Technology of China.

Acknowledgments

I would like to express my special and tremendous thanks to my advisor, Professor Chi-Wang Shu. With his encouragement, his inspiration, and his great efforts to explain things clearly and simply, he helped to make this thesis possible. He is not only a mentor to me, but also a good friend.

I also want to deeply thank Professor Weinan E and Professor Xiantao Li for introducing me to the field of multiscale solid mechanics and giving me great help and valuable advice.

My thanks also go to Professor David Gottlieb, Professor Jan S. Hesthaven and Professor Constantine M. Dafermos for teaching me the courses and sharing their knowledge selflessly.

I also want to thank my fellows and friends Fengyan Li, Shanqin Chen, Ching-Shan Chou, Yulong Xing, Ling Yuan, Jingmei Qiu, Yingda Cheng, Ishani Roy, Xiangxiong Zhang, Bo Dong, Yanlai Chen and Bian Qian for their support and help in my graduate study.

I would like to express my appreciation to the supporting staff in the Division of Applied Math for maintaining a friendly and stable environment.

Last, and most importantly, I wish to thank my parents, Junxiu Wang and Guiqin Liu. They always encourage me, support me, understand me and love me wherever and whenever I am. Without them, it would have been impossible for me to finish this work.

Contents

List of Tables

List of Figures

Chapter 1

Introduction

In the recent years, there have been many contributions to the development of discontinuous Galerkin (DG) methods for solving partial differential equations (PDEs) in various areas. The DG method is a finite element method which uses completely discontinuous piecewise basis functions and relies on an adequate choice of numerical fluxes to handle effectively the interactions across element boundaries, to achieve stable and accurate algorithms. Stable and convergent DG methods have been designed for linear and nonlinear PDEs. For example, the Runge Kutta discontinuous Galerkin method (RKDG) for hyperbolic conservation laws was introduced by Cockburn and Shu in [30, 32]. One extension, the local discontinuous Galerkin method (LDG), was carried out for solving convection-diffusion equations in [31] and dispersive wave equations in [73]. An introduction to DG methods for elliptic equations is given by Arnold, Brezzi, Cockburn and Marini in [9]. A minimal dissipation LDG (MD-LDG) method has been designed for elliptic equations in [25]. A multiscale DG method based on non-polynomial approximation spaces has been developed in [74, 75]. We also refer to the reader to [33] for a review of the DG methods.

DG schemes have several important advantages. Comparing with the finite difference methods, the DG methods are better suited to handle complicated geometries and boundary conditions and it is easier to achieve high order accuracy. Compar-

ing with traditional Galerkin methodology (e.g., [45]), the advantages of the DG methods includes their flexibility in h-p adaptivity and parallel efficiency.

We will present the following three topics in this thesis.

- The discontinuous Galerkin method for the multiscale modeling of dynamics of crystalline solids.
- The WKB local discontinuous Galerkin method for the simulation of the Schrödinger equation in a resonant tunneling diode.
- A multiscale DG method for solving a class of second order elliptic problems with rough coefficients.

These topics concern the applications of the DG method to different areas. We take advantage of the properties of the DG method to develop special methods to different problems. For example, in the first topic, we use a locally curl-free function space for the deformation gradient which can provide a coherent displacement field, following the local structure preserving DG methodology in [28, 52]. We compare the DG results with a second order Lax-Friedrichs type central scheme [60]. The DG methods show their advantage in the ability to resolve sharp wave fronts. In the second topic, we present a WKB-LDG method to solve the Schrödinger equation, which is in essence an LDG method based on exponential basis functions in the spirit of [74]. The method maintains the advantages of the general DG/LDG methods and saves in computational cost as well as memory when compared with the regular polynomial-based LDG methods. More importantly, it is feasible to extend the WKB-LDG method to two-dimensional devices which is impossible for traditional finite element method. In the third topic, for problems with oscillatory coefficients involving a small scale, the standard DG methods using polynomial spaces require a very fine mesh to resolve the small scale in the solution. We proposed a DG method based on special approximation spaces which are constructed to well approximate

the solution. Then this multiscale DG method allows the use of a coarse mesh and saves computational cost.

Chapter 2

The Discontinuous Galerkin Methods

In this chapter, we will review the version of DG methods developed by Cockburn et al. We will briefly review the DG method for 1-D scalar hyperbolic and the LDG method for parabolic equations in the first section. For more details, we refer the reader to the series of papers of Cockburn et al. [30, 29, 26, 32], the lecture notes [24] and the review paper [33]. The LDG [9] and MD-LDG methods [25] for 1-D elliptic equations will be briefly discussed in the second section.

2.1 Formulations for 1-D scalar hyperbolic and parabolic equations

We consider a one-dimensional conservation law on a given interval $I = [a, b]$:

$$u_t + f(u)_x = 0.$$

The interval I is divided into N cells as follows,

$$a = x_{\frac{1}{2}} < x_{\frac{3}{2}} < \ldots < x_{N+\frac{1}{2}} = b. \tag{2.1}$$

We denote

$$I_i = (x_{i-\frac{1}{2}}, x_{i+\frac{1}{2}}), \quad x_i = \frac{1}{2}(x_{i-\frac{1}{2}} + x_{i+\frac{1}{2}}) \tag{2.2}$$

and

$$\triangle x_i = x_{i+\frac{1}{2}} - x_{i-\frac{1}{2}}, \quad h = \max_i \triangle x_i. \tag{2.3}$$

Next, we define the approximation space as

$$V_h^k = \{v_h : (v_h)|_{I_i} \in P^k(I_i), i = 1, \ldots, N\}. \tag{2.4}$$

Here $P^k(I_i)$ denotes the set of all polynomials of degree at most k in the interval I_i. For simplicity, we will use the notation u and v instead of u_h, v_h to denote the numerical solutions whenever this does not cause confusion. We can choose a basis of $P^k(I_i)$ as, for example, $\{1, \xi_i, \ldots, \xi_i^k\}$, where the monomials $\xi = \frac{x - x_i}{\triangle x_i}$. For a function $v \in V_h^k$, we use $v_{i+\frac{1}{2}}^-$ and $v_{i+\frac{1}{2}}^+$ to refer to the left and right limits of v at $x_{i+\frac{1}{2}}$, respectively, at the interface where v is discontinuous.

The formulation of the DG method is as follows: find $u(., t) \in V_h^k$ such that for any test functions $v \in V_h^k$,

$$\int_{I_i} u_t v dx - \int_{I_i} f(u) v_x dx + \widehat{f(u)}_{i+\frac{1}{2}} v_{i+\frac{1}{2}}^- - \widehat{f(u)}_{i-\frac{1}{2}} v_{i-\frac{1}{2}}^+ = 0. \tag{2.5}$$

The single-valued flux $\hat{f}_{i+\frac{1}{2}}$ should be taken as a monotone flux depending on both $u_{i+\frac{1}{2}}^-$ and $u_{i+\frac{1}{2}}^+$ (exact or approximate Riemann solvers in the system case); see, for example, [51]. We will choose the numerical fluxes to be the Lax-Friedrichs flux

$$\hat{f}_{i+\frac{1}{2}} = \frac{1}{2}(f_{i+\frac{1}{2}}^- + f_{i+\frac{1}{2}}^+ - \alpha(u_{i+\frac{1}{2}}^+ + u_{i+\frac{1}{2}}^-)), \tag{2.6}$$

where $\alpha = \max |f'(u)|$.

Time discretization is done by the nonlinearly stable high order TVD Runge-Kutta methods developed in [67]. In particular, the second- and third-order TVD Runge-Kutta methods are used to match the corresponding spatial accuracy in this thesis. For solving the method of the lines ODE

$$u_t = L(u), \tag{2.7}$$

where $L(u)$ can be any spatial discretization of u, the second-order TVD Runge-Kutta method is given by

$$\begin{aligned} u^{(1)} &= u^n + \triangle t L(u^n), \\ u^{n+1} &= \frac{1}{2}u^n + \frac{1}{2}u^{(1)} + \frac{1}{2}\triangle t L(u^{(1)}), \end{aligned} \tag{2.8}$$

and the third-order TVD Runge-Kutta method is given by

$$\begin{aligned} u^{(1)} &= u^n + \triangle t L(u^n), \\ u^{(2)} &= \frac{3}{4}u^n + \frac{1}{4}u^{(1)} + \frac{1}{4}\triangle t L(u^{(1)}), \\ u^{n+1} &= \frac{1}{3}u^n + \frac{2}{3}u^{(2)} + \frac{2}{3}\triangle t L(u^{(2)}). \end{aligned} \tag{2.9}$$

Since the DG method may have oscillations when the solutions contain discontinuities, nonlinear total variation bounded (TVB) limiters are often used. The limiter we use in this thesis is briefly described below. For more details we refer the readers to Shu [66], and Cockburn, Lin, and Shu [29], and Cockburn and Shu [32]. Denote

$$u^-_{i+\frac{1}{2}} = \bar{u}_i + \tilde{u}_i, \quad u^+_{i-\frac{1}{2}} = \bar{u}_i - \tilde{\tilde{u}}_i, \tag{2.10}$$

where $\bar{u}_i$ is the cell average. $\tilde{u}_i$ and $\tilde{\tilde{u}}_i$ are modified by

$$\tilde{u}_i^{(mod)} = m\left(\tilde{u}_i, \bar{u}_{i+1} - \bar{u}_i, \bar{u}_i - \bar{u}_{i-1}\right), \quad \tilde{\tilde{u}}_i^{(mod)} = m\left(\tilde{\tilde{u}}_i, \bar{u}_{i+1} - \bar{u}_i, \bar{u}_i - \bar{u}_{i-1}\right), \tag{2.11}$$

where the minmod function m is given by

$$m(a_1, a_2, \ldots, a_n) = \begin{cases} s \cdot \min_{1\le j\le n} |a_j| & \text{if sign}(a_1)=\ldots=\text{sign}(a_n)=\text{s}, \\ 0 & \text{otherwise}, \end{cases} \tag{2.12}$$

or by the TVB modified minmod function [66]

$$\tilde{m}(a_1, a_2, \ldots, a_n) = \begin{cases} a_1 & \text{if } |a_1| \le Mh^2, \\ m(a_1, a_2, \ldots, a_n) & \text{otherwise}, \end{cases} \tag{2.13}$$

where $M > 0$ is a constant. The choice of M depends on the solutions of the problem. For the scalar case, it is possible to estimate M (M is related to the magnitude of the second derivatives of the solution at smooth extrema); however, it is more difficult for systems. In this thesis, we apply the limiter to every component of the system with a suitable M (which may not necessarily be the optimal M).

In the case where diffusion terms are present, e.g., the convection-diffusion problems

$$u_t = (a(u, x)u_x)_x, \tag{2.14}$$

where $a(u, x) \ge 0$, the idea of the LDG method [31] is to rewrite (2.14) into a first order system

$$q - u_x = 0, \quad u_t - (a(u, x)q)_x = 0. \tag{2.15}$$

We can then formally use the same DG method for the convection equation to solve (2.15), resulting in the following scheme: find $u(., t), q(., t) \in V_h^k$ such that

$$\int_{I_i} qwdx + \int_{I_i} uw_x dx - \widehat{u}_{i+\frac{1}{2}} w^-_{i+\frac{1}{2}} + \widehat{u}_{i-\frac{1}{2}} w^+_{i-\frac{1}{2}} = 0, \tag{2.16}$$

$$\int_{I_i} u_t v dx + \int_{I_i} a(u,x) q v_x dx - \widehat{aq}_{i+\frac{1}{2}} v^-_{i+\frac{1}{2}} + \widehat{aq}_{i-\frac{1}{2}} v^+_{i-\frac{1}{2}} = 0 \tag{2.17}$$

for all test functions $v, w \in V_h^k$. In [31], criteria are given for the numerical fluxes to guarantee stability, convergence, and a suboptimal error estimate of order k in the L_2-norm for piecewise polynomials of degree k. A clever choice of the fluxes in an alternating way

$$\hat{u}_{i+\frac{1}{2}} = u^-_{i+\frac{1}{2}}, \quad \hat{q}_{i+\frac{1}{2}} = q^+_{i+\frac{1}{2}} \tag{2.18}$$

or

$$\hat{u}_{i+\frac{1}{2}} = u^+_{i+\frac{1}{2}}, \quad \hat{q}_{i+\frac{1}{2}} = q^-_{i+\frac{1}{2}} \tag{2.19}$$

would satisfy these criteria and give a scheme of order $k+1$.

2.2 Formulations for 1-D elliptic problems

We consider the following 1-D elliptic problem

$$\begin{aligned} &-(a(x)u_x)_x - c(x)u = f(x), \quad a < x < b, \\ &u(a) = 0, \ u(b) = 0, \end{aligned} \tag{2.20}$$

where $a(x) \geq 0$.

We first rewrite the problem (2.20) as a first order system

$$q - u_x = 0, \quad -(a(x)q)_x - c(x)u = f. \tag{2.21}$$

We use the same notations in Sec. 2.1. The general formulation of the DG method for the elliptic problem (2.20) is: find $u, q \in V_h^k$ such that

$$\int_{I_j} q w dx + \int_{I_j} u w_x dx - \widehat{u}_{j+\frac{1}{2}} w^-_{j+\frac{1}{2}} + \widehat{u}_{j-\frac{1}{2}} w^+_{j-\frac{1}{2}} = 0, \tag{2.22}$$

$$\int_{I_j} aq v_x dx - \widehat{aq}_{j+\frac{1}{2}} v^-_{j+\frac{1}{2}} + \widehat{aq}_{j-\frac{1}{2}} v^+_{j-\frac{1}{2}} - \int_{I_j} cuv dx = \int_{I_j} fv dx \tag{2.23}$$

for all test functions $v, w \in V_h^k$.

Different choices of numerical fluxes produce different methods. For example, the flux formulation of the LDG method [20, 27] is

$$\begin{aligned} \hat{u} = u^-, \quad \hat{q} = q^+ + \alpha[u] \quad \text{at the internal cell interfaces,} \\ \hat{u} = 0, \quad \widehat{q}_{N+\frac{1}{2}} = q^+_{N+\frac{1}{2}} + \alpha(u(b) - u^-_{N+\frac{1}{2}}) \quad \text{at the boundaries;} \end{aligned} \tag{2.24}$$

or

$$\begin{aligned} \hat{u} = u^+, \quad \hat{q} = q^- + \alpha[u] \quad \text{at the internal cell interfaces,} \\ \hat{u} = 0, \quad \widehat{q}_{\frac{1}{2}} = q^+_{\frac{1}{2}} + \alpha(u^+_{\frac{1}{2}} - u(a)) \quad \text{at the boundaries.} \end{aligned} \tag{2.25}$$

Here $[u] = u^+ - u^-$ and $\alpha = O(1/h)$.

The MD-LDG method [25] we will use in this thesis has a flux formulation

$$\begin{aligned} \hat{u} = u^-, \quad \hat{q} = q^+ \quad \text{at the internal cell interfaces,} \\ \hat{u} = 0, \quad \widehat{q}_{N+\frac{1}{2}} = q^+_{N+\frac{1}{2}} + \alpha(u(b) - u^-_{N+\frac{1}{2}}) \quad \text{at the boundaries;} \end{aligned} \tag{2.26}$$

or

$$\begin{aligned} \hat{u} = u^+, \quad \hat{q} = q^- \quad \text{at the internal cell interfaces,} \\ \hat{u} = 0, \quad \widehat{q}_{\frac{1}{2}} = q^+_{\frac{1}{2}} + \alpha(u^+_{\frac{1}{2}} - u(a)) \quad \text{at the boundaries,} \end{aligned} \tag{2.27}$$

We get optimal convergence for both u and q in one dimension, and optimal convergence for u but suboptimal convergence for q in two dimensions.

Chapter 3

The Discontinuous Galerkin Method for the Multiscale Modeling of Dynamics of Crystalline Solids

3.1 Introduction

The conventional computational methods for solid mechanics have been primarily based on continuum models, where one uses a small number of variables, such as the strain and stress, to efficiently describe the mechanical properties. The quality of these continuum models depends heavily on the constitutive assumptions, which are usually obtained from experimental observations. On the other hand, atomistic models, such as molecular statistics and molecular dynamics (MD), which account for detailed crystal structure and atomic configurations, have been proven to be a useful methodology. However, to model a macroscale process, such atomistic systems are too large to fit into a realistic computation. Therefore, it is computationally advantageous to develop a hybrid model that includes both components. Multiscale

methods that aim to bridge different scales have been an active area of interest. Recently developed methods in this class include, for instance, the quasicontinuum methods [68, 49], the macro atomistic ab initio dynamics method [6], the bridging scale method [71], the bridging domain methods [72], the heterogeneous multiscale method (HMM) [39, 53, 40], and the pseudo-spectral method [69]. The advantage of such concurrent methods is that the models can be refined as the computation proceeds.

This chapter is concerned with the dynamics of elastic solids. We will use the framework of HMM [39, 53]. The main idea of HMM is to formulate both the atomistic and continuum models in terms of universal conservation laws, and the coupling is accomplished by ensemble averaging. The implementation of such a method consists of three components:

1. a macrosolver for the continuum model,

2. a microsolver to equilibrate the atomistic system locally to the appropriate ensemble,

3. an averaging procedure to obtain data that are needed in the continuum model.

The main advantage of this formalism is that one is able to use the macroscale equations to capture the elastic waves, and the microscale models are employed as a supplemental component to provide accurate constitutive data, thereby bypassing any empirical model for the equation of state.

The constitutive relation obtained from the atomistic models is typically nonlinear and temperature dependent. As a result, shock waves may develop, which give rise to large strain and velocity gradients, posing a great challenge to numerical simulations. In addition suitable constraints have to be imposed to form a coherent displacement field. The problem is further complicated by the presence of defects, causing large local deformations and discontinuities in strain and displacement. To overcome these difficulties, we will make use of the DG method, a finite element

method based on piecewise polynomials as basis functions that are completely discontinuous across element boundaries. The DG method will be formulated for the elastodynamics problems in the multiscale setting.

We remark that, in the recent years, there have been many contributions to the development of DG methods for solving PDEs in solid mechanics. In most cases, attention has been restricted to linear elasticity problems. For example, Rivière et al. [65] formulated and analyzed a DG method for linear elasticity based on a generalization of the nonsymmetric interior penalty DG method for the diffusion equation. Käser and Dumbser (see [47, 38]) proposed a DG method in space that uses the arbitrary high-order derivatives (ADER) approach for the time integration to solve the linear elastic wave equation in heterogeneous media on unstructured meshes in two and three dimensions. Huang and Costanzo (see [44, 35]) proposed a space-time DG formulation for linear elasticity where stress discontinuities were considered through jumps in the material properties, see also [48]. Abedi, Petracovici, and Haber [5] proposed a space-time DG method for linearized elastodynamics that delivered an exact balance of linear and angular momentum over every space-time element.

In this chapter we are going to present a multiscale methodology for transient elastodynamics problems based on the DG method as a macrosolver. We will discuss how the DG method can be used to capture a large scale elastic field and how the MD can be used at the atomic scale and coupled to the macroscale DG solver to provide accurate constitutive data. We do recognize, however, that the constitutive behavior of realistic materials usually results from complicated interactions of local defects, such as dislocations, cracks, grain boundaries etc. In this case, the stress-strain relation cannot simply be deduced from the Cauchy-Born rule or thermodynamics of a single crystal. Nonetheless, the current method is applicable to small systems, e.g., micromechanical system, where only a small number of defects are present. There the DG method, coupled with equilibrium MD, becomes useful in regions away from the defects, which in the quasicontinuum method [68, 49], has been referred to as the

local region. On one hand, it offers an accurate solver for the stress waves, providing loading condition on the material defects. On the other hand, mesh refinement can easily be done as one approaches the atomistic region. Our next step is to combine the current method with nonequilibrium MD to describe defect formation and propagation.

3.2 Macroscopic and microscopic models

Our computation involves models at both macroscopic and microscopic scales: elastodynamics on the macroscopic scale, describing the evolution of the elastic field, and molecular dynamics at the atomic scale, providing the constitutive data based on detailed atomic interactions. In this section, we briefly present the equations underlying these models.

On the continuum scale, the governing equations for the elastodynamics are a set of PDEs. To begin with, we fix a reference coordinate, denoted by $\mathbf{x}$, and after deformation, the point will be displaced to a new position, $\mathbf{x}+\mathbf{u}(\mathbf{x},t)$, with $\mathbf{u}$ being the displacement. Let $\varepsilon = \nabla\mathbf{u}$ be the corresponding deformation gradient. Then the continuum equations take the form:

$$\begin{cases} \frac{\partial}{\partial t}\varepsilon - \nabla\mathbf{v} &= 0, \\ \rho_0\frac{\partial}{\partial t}\mathbf{v} - \nabla\cdot P &= 0, \\ \rho_0\frac{\partial}{\partial t}e + \nabla\cdot\mathbf{j} &= 0. \end{cases} \tag{3.1}$$

Here $\mathbf{v}$ and e are the velocity and specific energy per particle, respectively, ρ_0 is the initial density, P is the first Piola-Kirchhoff stress tensor and $\mathbf{j}$ is the energy flux. The first equation in (3.1) describes the time evolution of the deformation; the second and third equations reflect conservation of momentum and energy, respectively. In continuum mechanics, for instance [50], these equations are supplemented by the empirical constitutive relations for stress and energy fluxes. The purpose of our

work is to develop multiscale strategies that bypass these empirical constitutive laws when their accuracy is in doubt.

At the atomic scale, the motion of the atoms constituting the solids is given by molecular dynamics,

$$\begin{cases} \dot{\mathbf{q}}_i &= \mathbf{p}_i/m_i, \\ \dot{\mathbf{p}}_i &= -\nabla_{\mathbf{q}_i} V, \end{cases} \tag{3.2}$$

where m_i denotes the mass of the ith atom, $\mathbf{q}_i$ and $\mathbf{p}_i$ are the generalized coordinate and momentum for the ith atom, and $V(\mathbf{q}_1, \mathbf{q}_2, \ldots, \mathbf{q}_N)$ is the interatomic potential that models the interaction among the atoms. In this work, we will only consider pair potential. Namely,

$$V = \frac{1}{2}\sum_{i \neq j} \phi(r_{ij}), \quad r_{ij} = |\mathbf{r}_{ij}|, \quad \mathbf{r}_{ij} = \mathbf{q}_i - \mathbf{q}_j.$$

Many-body potential models, such as the embedded atom model (EAM) [37] and Tersoff-Brenner model [70], can be dealt with similarly. The system (3.2) is a Hamiltonian system with the Hamiltonian

$$H(\mathbf{q}, \mathbf{p}) = \sum_i \frac{\mathbf{p}_i^2}{2m_i} + V(\mathbf{q}), \ \mathbf{q} = (\mathbf{q}_1, \mathbf{q}_2, \ldots, \mathbf{q}_N), \mathbf{p} = (\mathbf{p}_1, \mathbf{p}_2, \ldots, \mathbf{p}_N). \tag{3.3}$$

The basic assumption in our current method is scale separation. Namely the relaxation time for the microscopic processes is much shorter than the typical time scale of the continuum. In this case, it suffices to consider the local equilibrium distribution of the atomistic system. In the case of zero temperature, this is equivalent to the Cauchy-Born hypothesis, which suggests that the atomic displacement follow the macroscopic deformation. As a result, the strain energy density and elastic stress can be computed from the atomistic models. At finite temperature, one has to take into account the thermal fluctuation and compute elastic properties based on statistical ensembles. In this work, we consider two statistical equilibrium: the microcanonical

distribution,

$$\rho_1(\mathbf{q},\mathbf{p}) = \frac{1}{Z}\delta(E-H), \tag{3.4}$$

where the volume and the energy of the system are prescribed, and the canonical distribution,

$$\rho_2(\mathbf{q},\mathbf{p}) = \frac{1}{Z}e^{-\beta H}, \quad \beta = (k_B T)^{-1} \tag{3.5}$$

where the volume and the temperature are given. The constant Z, which is the partition function, normalizes the probability density. Although these statistical ensembles in principle are equivalent in the infinite volume limit, one might have more practical convenience than the other. Once the equilibrium distribution is available, physical observables can be computed via statistical averaging. More specifically, let w be any observable with a microscopic expression $w(\mathbf{q},\mathbf{p})$. Then

$$\langle w \rangle = \int w(\mathbf{q},\mathbf{p})\rho(\mathbf{q},\mathbf{p})d\mathbf{q}d\mathbf{p}. \tag{3.6}$$

In a MD simulation, we can replace the ensemble average by a time average,

$$\langle w \rangle = \lim_{T\to\infty}\frac{1}{T}\int_0^T w(\mathbf{q}(t),\mathbf{p}(t))dt, \tag{3.7}$$

provided that the system is ergodic.

The remaining step in the atomic/continuum coupling is to define the corresponding macroscopic quantities at the atomic scale. Since the continuum equations (3.1) are expressed in the Lagrangian coordinate, we first define the reference coordinate for the atoms as the equilibrium positions, denoted by Q_i. Next we will mainly focus on the calculation of the stress tensor. The first approach to define stress from the atomic scale is from thermodynamics [17]. For the atomistic system, the free energy is defined as,

$$\mathcal{F} = -k_B T \ln \int e^{-\beta H} d\mathbf{q}d\mathbf{p}.$$

Implicit in the integral is the dependence on the deformation gradient ε, which

changes the volume and shape of the entire system. Here periodic boundary condition is assumed. From the second law of thermodynamics, we have,

$$\frac{1}{\Omega}\frac{\partial \mathcal{F}}{\partial \varepsilon} = P,$$

fixing the temperature. Here Ω is the volume of the system in the reference coordinate. This calculation yields,

$$P = \frac{1}{\Omega}\sum_{i<j}\phi'(r_{ij})\frac{\mathbf{r}_{ij}\otimes Q_{ij}}{r_{ij}^2}, \quad Q_{ij} = Q_i - Q_j. \tag{3.8}$$

A more natural approach to derive the microscopic expressions is based on conservation laws at the atomic scale [46]. More specifically, we define the local momentum and energy

$$\begin{cases} \widetilde{\mathbf{q}}(\mathbf{x},t) &= \sum_i \mathbf{q}_i(t)\delta(\mathbf{x}-Q_i), \\ \widetilde{e}(\mathbf{x},t) &= \frac{1}{2}\sum_i \Big[\frac{\mathbf{p}_i^2}{m_i} + \sum_{j\neq i}\phi\big(\mathbf{q}_i(t)-\mathbf{q}_j(t)\big)\Big]\delta(\mathbf{x}-Q_i). \end{cases} \tag{3.9}$$

As a result, the total momentum and energy in a control volume can be easily computed. Furthermore, one can derive conservation laws for the local momentum and energy,

$$\begin{cases} \frac{\partial}{\partial t}\widetilde{\mathbf{q}} - \nabla\cdot\widetilde{P} &= 0, \\ \rho_0\frac{\partial}{\partial t}\widetilde{e} + \nabla\cdot\widetilde{\mathbf{j}} &= 0. \end{cases} \tag{3.10}$$

where,

$$\begin{cases} \widetilde{P}(\mathbf{x},t) &= \frac{1}{2}\sum_{i\neq j}\phi'\big(\mathbf{q}_i-\mathbf{q}_j\big)\otimes(Q_i-Q_j) \\ &\times \int_0^1 \delta\big(\mathbf{x}-(\mathbf{Q}_j+\lambda(Q_i-Q_j))\big)d\lambda, \\ \widetilde{\mathbf{j}}(\mathbf{x},t) &= \frac{1}{4}\sum_{i\neq j}\big(\mathbf{p}_i/m_i+\mathbf{p}_j/m_j\big)\cdot\phi'\big(\mathbf{q}_i-\mathbf{q}_j\big)\otimes(Q_i-Q_j) \\ &\times \int_0^1 \delta\big(\mathbf{x}-(Q_j+\lambda(Q_i-Q_j))\big)d\lambda. \end{cases} \tag{3.11}$$

Averaging (3.11) in space, one also arrives at (3.8).

Equations (3.1) and (3.10) have been the starting point of HMM: the continuum and atomistic models can be coupled at the level of conservation laws. Such observation is also reminiscent of the concept of local equilibrium in the kinetic theory for gas dynamics, where the Maxwellian distribution can be used to provide the equation of state, and therefore close the continuum equations.

3.3 Numerical methodology

3.3.1 Macroscale solver: the DG method

In this chapter, we solve the continuum equations (3.1) as a one-dimensional system of conservation laws. We will use the DG method and the LDG method which are described in Chap. 2 as our macroscale solver.

3.3.2 MD simulation

In computing the elastic stress from the microscopic model, we prepare the atomistic system as follows. We first arrange the atoms to the equilibrium position, Q_j, and then apply a uniform deformation, $\mathbf{q}_j = (I+A)Q_j$. The major axes of the simulation box are also deformed accordingly. Periodic boundary conditions are applied

with respect to the deformed box to maintain the deformation gradient throughout the computation. The initial velocity for the atoms is sampled from a Gaussian distribution with the variance given by $k_B T$. In order to maintain the system at a given temperature, we use the standard Nosé-Hoover thermostat [61, 43]. To ensure numerical stability, the time step is chosen so that $\delta t \leq 2/\omega_{max}$, where ω_{max} is the largest phonon frequency. During the simulation, the stress is sampled every 20 time steps, and then averaged at the end of the simulation according to (3.7). In addition the Verlet list method is used to speed up the force calculation. These standard techniques can be found in [41].

3.3.3 The multiscale method

Having described the methodology for solving the atomistic and continuum equations, we are now in a position to describe the multiscale method. The coupling strategy is quite straightforward: we first divide the computational domain into cells over which the macroscale equations (3.1) are discretized. In computing the numerical fluxes, the stress and heat flux are obtained directly from the atomistic model, either from a MD simulation, or from a simplified model, also calibrated from atomistic simulations beforehand (see next section). This procedure can be demonstrated in Fig. 3.1. Comparing to the conventional numerical procedure, we have used an atomistic model as a supplemental component on each cell to supply the constitutive data.

3.4 One-dimensional shock propagation

In our first example the system is described at the atomistic level by a Lennard-Jones potential:

$$\phi(r) = 4\varepsilon \left(\left(\frac{\sigma}{r}\right)^{12} - \left(\frac{\sigma}{r}\right)^{6} \right). \tag{3.12}$$

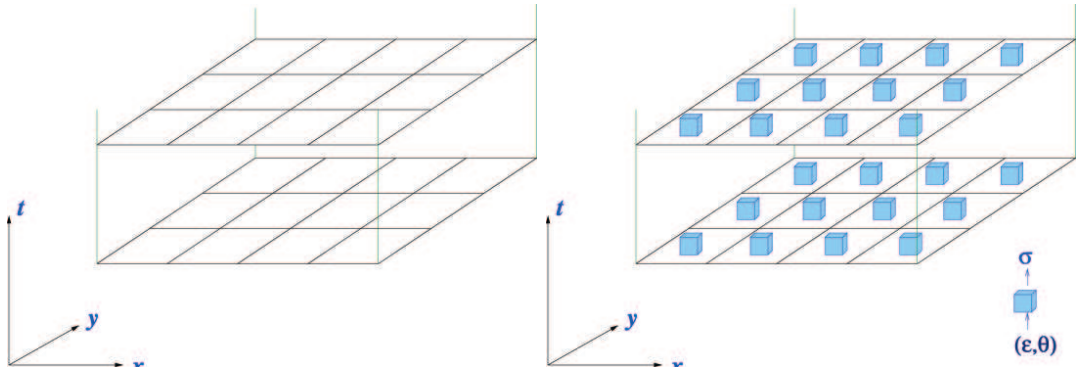

Figure 3.1: Left: conventional numerical methods; Right: the heterogeneous multiscale methods. In the multiscale method, an additional component, indicated by the small boxes, is applied to compute the elastic stress. Here $\theta = k_B T$.

All the particles are assumed to have mass m. In the MD simulation, the parameters ε and σ are normalized to unit. As a result, all the computational results are expressed in terms of reduced units, represented by m, ε and σ. The atomistic system is two-dimensional and it is constrained to a narrow slab so that the macroscopic dynamics is essentially one-dimensional. The continuum equations then reduce to

$$\begin{cases} \partial_t \varepsilon_{11} - \partial_x v_1 &= 0, \\ \rho_0 \partial_t v_1 - \partial_x P_{11} &= 0, \\ \rho_0 \partial_t e - \partial_x (P_{11} v_1) &= 0. \end{cases} \tag{3.13}$$

The initial condition for the macroscale quantities is set up as follows: For the $x < 0$ half plane, we impose a uniform deformation gradient $\varepsilon_{11} = -0.01$, and for the other half plane, the deformation gradient is zero. The system starts from zero velocity and the temperature $T = 0.1$ on the left half plane, and $T = 0.3$ on the right half plane. From the continuum viewpoint, this is an example of the Riemann problem.

We apply the multiscale procedure described above to this problem with the DG method as the macroscale solver. The P^1 and P^2 (second and third order based on piecewise linear and quadratic polynomials) DG results are presented. The numerical results are shown in Fig. 3.2. As a comparison, we also compute the solution with the

second-order Lax-Friedrichs type central schemes, described in Nessyahu and Tadmor [60]. At $t > 0$, one observes two shocks separated by a contact discontinuity. We can see that the DG method captures the discontinuities very well. This type of results have also been confirmed by a full atomistic simulation [53].

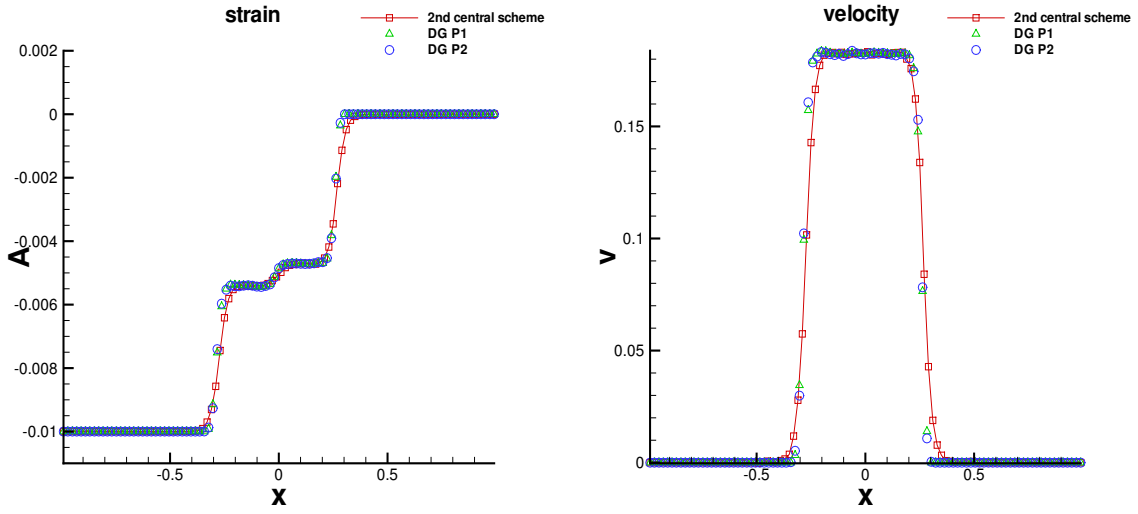

Figure 3.2: Numerical test on 1-D shock formation and propagation. 100 macrocells are used. The solutions are displayed at the physical time $T = 0.01$. Solid line with the square symbol: the second-order central scheme; triangle and circle symbols: DG P^1 and P^2 with TVD limiter. Left: strain, right: velocity.

3.5 Two-dimensional case

In our next simulation, the atomistic model is a three-dimensional Lennard-Jones solid with the face-centered cubic (FCC) structure. The major axes of the system are along the (100), (010), (001) directions. We consider a system in a state of plain strain so that the macro scale behavior is essentially two-dimensional.

3.5.1 Atomistic-based constitutive models

The energy flux $\mathbf{j}$ in the continuum equations (3.1) can be written as

$$\mathbf{j} = -(\mathbf{v}^T P + \mathbf{q}), \tag{3.14}$$

with $\mathbf{q}$ being the heat flux.

In principle the heat flux can be computed from an atomistic simulation with a consistent temperature gradient [53]. However such simulations typically take much longer time to relax, making the computation rather expensive. Other models, such as the kinetic equation for phonons [62], are available. But it is not yet clear how those models can be coupled with MD or elastodynamics. For simplicity, we model the heat flux by the Fourier law,

$$\mathbf{q} = \kappa \nabla T, \tag{3.15}$$

which has been confirmed via numerous numerical studies [18]. The heat conductivity has been precomputed from the atomistic model. In the following computations, we will consider both the case with the heat flux as well as the one without the heat flux.

In the case of small deformations and a low temperature, a linear approximation can be made to provide an explicit stress strain relation:

$$P_{ij} = c_{ijkl}\varepsilon_{kl} + \alpha T \delta_{ij} \quad i,j,k,l = 1,2 \tag{3.16}$$

where c_{ijkl} are elastic parameters. They can be computed directly from the atomistic

model [10]. In particular, we have

$$\begin{cases} P_{11} &= C_{11}\varepsilon_{11} + C_{12}\varepsilon_{22} + \alpha T, \\ P_{12} &= C_{44}(\varepsilon_{12} + \varepsilon_{21}), \\ P_{21} &= P_{12}, \\ P_{22} &= C_{11}\varepsilon_{22} + C_{12}\varepsilon_{11} + \alpha T. \end{cases} \tag{3.17}$$

In terms of the reduced units, these parameters have been obtained from the atomistic model,

$$C_{11} = 97.56753, \quad C_{12} = 55.56524, \quad C_{44} = 55.55364,$$

$$\alpha = -9.91139, \quad \kappa = 0.1925353265.$$

It has been calibrated such that under the condition,

$$\|\varepsilon\|_2 < 0.004 \quad \text{and} \quad T < 0.2, \tag{3.18}$$

the error of this linear approximation (3.17) is within one percent. However this model cannot be directly used because in the PDEs the temperature is not a derived quantity and needs to be obtained from the atomistic models. For this purpose we make another approximation for the temperature,

$$\rho_0 e = E(\varepsilon, T) = E_0 + \frac{1}{2} c_{ijkl}\varepsilon_{kl}\varepsilon_{ij} + 3T. \tag{3.19}$$

Here the first term is the cohesive energy of the crystalline, $E_0 = -7.4591$ per atom, the second term is the familiar form of the strain energy for linear elasticity. In the case of low energy, namely,

$$|E - E_0| < 1.2, \tag{3.20}$$

the modeling error for this approximation (3.19) is also within one percent.

The equations (3.17) and (3.19) provide an efficient constitutive model in the regime of small strain and low temperature. We will show that with these constitutive equations, the system of PDEs is hyperbolic. With the heat flux $\mathbf{q}$ present, the system is of parabolic type.

3.5.2 The hyperbolicity of the constitutive model without the heat flux

When the deformation is small and the temperature is low, we can use the linearized stress strain relation (3.17) and the linearized temperature relation (3.19) to solve for the temperature T, to obtain a closed system of equations. For the case without the heat flux, this system of equations can be written in the form of a system of conservation laws:

$$\mathbf{U}_t + \mathbf{F}_x + \mathbf{G}_y = 0,$$

where

$$\mathbf{U} = \begin{pmatrix} \varepsilon_{11} \\ \varepsilon_{12} \\ \varepsilon_{21} \\ \varepsilon_{22} \\ \rho_0 v_1 \\ \rho_0 v_2 \\ \rho_0 e + \frac{1}{2}\rho_0(v_1^2 + v_2^2) \end{pmatrix}, \ \mathbf{F} = \begin{pmatrix} -v_1 \\ 0 \\ -v_2 \\ 0 \\ -P_{11} \\ -P_{21} \\ -v_1 P_{11} - v_2 P_{21} \end{pmatrix}, \ \mathbf{G} = \begin{pmatrix} 0 \\ -v_1 \\ 0 \\ -v_2 \\ -P_{21} \\ -P_{22} \\ -v_1 P_{21} - v_2 P_{22} \end{pmatrix} \tag{3.21}$$

with the relations (3.17) and (3.19).

It is known ([36] p.55), that the system (3.21) is hyperbolic on a certain region of the state space if, for every (ε, η) lying in that region, the following two conditions hold,

$$\frac{\partial \hat{E}(\varepsilon, \eta)}{\partial \eta} > 0, \tag{3.22}$$

$$\frac{\partial^2 \hat{E}(\varepsilon,\eta)}{\partial\varepsilon_{ij}\partial\varepsilon_{kl}}\nu_j\nu_l\xi_i\xi_k > 0, \quad \text{for all } \nu \text{ and } \xi, \tag{3.23}$$

where η is the entropy and $\hat{E}(\varepsilon,\eta) = E(\varepsilon,T)$. The first condition ensures that the temperature is positive, and the second condition, often referred to as the rank-one convexity condition, implies that the local thermal equilibrium is stable.

To compute the entropy $\eta = \eta(\varepsilon,T)$, using the Helmholtz free energy ([36], p.41)

$$\psi(\varepsilon,T) = e(\varepsilon,T) - T\eta, \tag{3.24}$$

we obtain

$$P_{ij} = \rho_0\frac{\partial\psi}{\partial\varepsilon_{ij}} = \frac{\partial E(\varepsilon,T)}{\partial\varepsilon_{ij}} - \rho_0 T\frac{\partial\eta}{\partial\varepsilon_{ij}} = c_{ijkl}\varepsilon_{kl} - \rho_0 T\frac{\partial\eta}{\partial\varepsilon_{ij}}. \tag{3.25}$$

The last equality comes from the expression of $E(\varepsilon,T)$ given by (3.19).

Applying the definition of P in (3.16) to (3.25) , we get

$$\rho_0 T\frac{\partial\eta}{\partial\varepsilon_{ij}} = -\alpha T\delta_{ij}. \tag{3.26}$$

Thus

$$\eta = -\frac{\alpha}{\rho_0}(\varepsilon_{11}+\varepsilon_{22}) + \varphi(T). \tag{3.27}$$

To determine the function $\varphi(T)$, we know from (3.24),

$$\eta(\varepsilon,T) = -\frac{\partial\psi}{\partial T} = -\frac{\partial(e-T\eta)}{\partial T} = -\frac{\partial e}{\partial T} + \eta + T\frac{\partial\eta}{\partial T} = -\frac{3}{\rho_0} + \eta + T\frac{\partial\eta}{\partial T}, \tag{3.28}$$

which then reduces to

$$T\frac{\partial\eta}{\partial T} = \frac{3}{\rho_0}. \tag{3.29}$$

Together with (3.27), we finally obtain the entropy for the system (3.21),

$$\eta(\varepsilon, T) = -\frac{\alpha}{\rho_0}(\varepsilon_{11} + \varepsilon_{22}) + \frac{3}{\rho_0}\log T \tag{3.30}$$

up to a constant.

Next , $\hat{T} = \hat{T}(\varepsilon, \eta)$ can be solved by (3.30),

$$\hat{T}(\varepsilon, \eta) = e^{(\rho_0\eta + \alpha(\varepsilon_{11}+\varepsilon_{22}))/3}. \tag{3.31}$$

Then

$$\hat{E}(\varepsilon, \eta) = E_0 + \frac{1}{2}c_{ijkl}\varepsilon_{kl}\varepsilon_{ij} + 3e^{(\rho_0\eta + \alpha(\varepsilon_{11}+\varepsilon_{22}))/3}. \tag{3.32}$$

For the first condition given by (3.22),

$$\frac{\partial \hat{E}(\varepsilon, \eta)}{\partial \eta} = \rho_0 e^{(\rho_0\eta + \alpha(\varepsilon_{11}+\varepsilon_{22}))/3} > 0. \tag{3.33}$$

The second condition (3.23), called the Legendre-Hadamard condition, means that $\hat{E}$ is rank-one convex in ε. It is equivalent to the condition that the matrix $\left(\frac{\partial^2 \hat{E}(\varepsilon,\eta)}{\partial\varepsilon_{ij}\partial\varepsilon_{kl}}\right)_{4\times 4}$ is positive definite.

It is easy to check that the matrix

$$\left(\frac{\partial^2 \hat{E}(\varepsilon,\eta)}{\partial\varepsilon_{ij}\partial\varepsilon_{kl}}\right)_{4\times 4} =$$

$$\begin{pmatrix} C_{11} + \frac{1}{3}\alpha^2 e^{(\rho_0\eta+\alpha(\varepsilon_{11}+\varepsilon_{22}))/3} & 0 & 0 & C_{12} + \frac{1}{3}\alpha^2 e^{(\rho_0\eta+\alpha(\varepsilon_{11}+\varepsilon_{22}))/3} \\ 0 & C_{44} & C_{44} & 0 \\ 0 & C_{44} & C_{44} & 0 \\ C_{12} + \frac{1}{3}\alpha^2 e^{(\rho_0\eta+\alpha(\varepsilon_{11}+\varepsilon_{22}))/3} & 0 & 0 & C_{11} + \frac{1}{3}\alpha^2 e^{(\rho_0\eta+\alpha(\varepsilon_{11}+\varepsilon_{22}))/3} \end{pmatrix} \tag{3.34}$$

is positive definite.

Therefore, the system (3.21) is hyperbolic.

3.5.3 Implementation of the constitutive models

While the equilibrium MD in principle offers the correct constitutive equation, such a procedure is typically computationally intensive, making the overall computation rather expensive. On the other hand, the simplified models in Sec. 3.5.1 are efficient, but the accuracy can only be guaranteed under small deformation and low temperature. Therefore it is computationally attractive to include both these models in the simulation: we use the constitutive relation (3.17) if the criterion (3.18) is met, and (3.19) if the condition (3.20) is satisfied; otherwise the data are obtained directly from a MD simulation. This resembles a Domain Decomposition Method (DDM) [21]. The main idea of the DDM is to solve the relatively inexpensive macroscopic model in most part of the computational domain, and only solve the micro problems in the sub-domains where the macroscopic model is not valid.

More specifically, our computational domain can be decomposed into four types of sub-domains. These sub-domains are distinguished by whether the conditions (3.18) and/or (3.20) are satisfied. For example, the first type of sub-domains can be the one satisfying both (3.18) and (3.20). In this case, a computationally inexpensive macro model is sufficient, and we no longer need to do MD. The procedure of using the DDM is: at each time step and in each cell, if the energy is low, namely, if the condition (3.20) is satisfied, we will compute the temperature from (3.19) instead of the MD procedure. After the temperature is obtained, we compute the stress and energy flux from the atomistic model via a canonical ensemble. For small deformation and low temperature, i.e. when (3.18) holds, we use (3.17) to bypass the MD procedure.

In practice, we use parallel computing to speed up our program. At the macroscopic computational domain, for each time step, we first need to get the information of the temperature. We label the L cells to be those which satisfy the condition (3.20), and the H cells to be those in which this condition is not satisfied. Then we use the macro relation (3.19) to get the temperature in the L cells. This requires only a negligible cost comparing to MD. For the H cells, we do need to use MD with the

canonical ensemble (3.5), which are computationally expensive. To efficiently use all the processors, we collect all the H cells and distribute them to available processors evenly. Next, we need to get the information of the stress tensor. The procedure is the same as above, except that now the condition (3.18) and the relation (3.17) are used to distinguish different types of cells. This procedure is repeated for every macro time step.

3.5.4 Curl-free DG method

In the finite volume representation of the elastic field, it is important to ensure the kinematic compatibility at the cell interface. This issue has been recognized in [5]. In fact the macro scale PDEs are equipped with a natural constraint:

$$\nabla \times \varepsilon = 0,$$

which leads to two pairs of curl-free variables, $(\varepsilon_{11}, \varepsilon_{12})$ and $(\varepsilon_{21}, \varepsilon_{22})$. In order to fulfill the constraints, we choose a curl-free basis for our DG method instead of the standard polynomial basis. The original idea of using curl-free basis is from [28], in which the locally divergence-free DG method is designed to solve the Maxwell equations, and from [52], in which the locally curl-free DG method is designed to solve the Hamilton-Jacobi equations.

In the standard RKDG method, we seek the solution in the finite dimensional polynomial space

$$\bar{\mathbf{V}}_h^{7,k} = \left\{ \mathbf{v} = (v_1, v_2, v_3, v_4, v_5, v_6, v_7) : \mathbf{v}|_K \in \mathbf{P}^{7,k}(K), K \in \mathcal{K} \right\} \tag{3.35}$$

where K is the element and $\mathcal{K}$ is the collection of the elements, $\mathbf{P}^{7,k}(K) = (P^k(K))^7$, and $P^k(K)$ denotes the space of polynomials in K of degree at most k. Now we are

looking for the solution space which basis satisfies the curl-free condition, i.e.

$$\begin{aligned}
\mathbf{V}_h^k &= \left\{\mathbf{v} \in \bar{\mathbf{V}}_h^{7,k} : \tfrac{\partial v_1}{\partial y} = \tfrac{\partial v_2}{\partial x}\ ,\ \tfrac{\partial v_3}{\partial y} = \tfrac{\partial v_4}{\partial x}\right\} \\
&= \left\{\mathbf{v} = (v_1, v_2) \in \mathbf{P}^{2,k}(K) : \tfrac{\partial v_1}{\partial y} = \tfrac{\partial v_2}{\partial x}\right\} \\
&\oplus \left\{\mathbf{v} = (v_3, v_4) \in \mathbf{P}^{2,k}(K) : \tfrac{\partial v_3}{\partial y} = \tfrac{\partial v_4}{\partial x}\right\} \\
&\oplus \left\{\mathbf{v} = (v_5, v_6, v_7) : \mathbf{v} \in \mathbf{P}^{3,k}(K)\right\} \\
&= \mathbf{V}_h^{2,k} \oplus \mathbf{V}_h^{2,k} \oplus \bar{\mathbf{V}}_h^{3,k}
\end{aligned} \tag{3.36}$$

That is, the vectors (v_1, v_2) and (v_3, v_4) are curl-free polynomial vectors. Notice that the dimension of the space $\mathbf{V}_h^{2,k}$ is $(k+1)(k+4)/2$, only about half as the dimension of $\bar{\mathbf{V}}_h^{2,k}$ which is $(k+1)(k+2)$. Thus the total dimension of the curl free space $\mathbf{V}_h^k$ is (k^2+k) less than the standard piecewise polynomial space $\mathbf{V}_h^{7,k}$, and we can save a lot of computational cost by using the curl free space.

It is very easy to obtain the local bases for $\mathbf{V}_h^{2,k}$. We can take the gradient of the standard bases of $(P^{k+1}(K))$, since we know $\nabla \times \nabla f = 0$ for any scalar function f. For example, if K is the rectangle, with the center (x_i, y_j) and width $\triangle x_i$, $\triangle y_j$, if we denote

$$\xi = \frac{x - x_i}{\triangle x_i}, \quad \eta = \frac{y - y_j}{\triangle y_j},$$

then one set of bases of $\mathbf{V}_h^{2,k}$ would be, when $k = 1$,

$$\begin{pmatrix} 1 \\ 0 \end{pmatrix}, \begin{pmatrix} \xi \\ 0 \end{pmatrix}, \begin{pmatrix} \triangle y_j \eta \\ \triangle x_i \xi \end{pmatrix}, \begin{pmatrix} 0 \\ 1 \end{pmatrix}, \begin{pmatrix} 0 \\ \eta \end{pmatrix}. \tag{3.37}$$

For $k = 2$, we need to add

$$\begin{pmatrix} \xi^2 \\ 0 \end{pmatrix}, \begin{pmatrix} 2\triangle y_j \xi\eta \\ \triangle x_i \xi^2 \end{pmatrix}, \begin{pmatrix} \triangle y_j \eta^2 \\ 2\triangle x_i \xi\eta \end{pmatrix}, \begin{pmatrix} 0 \\ \eta^2 \end{pmatrix}. \tag{3.38}$$

And for $k = 3$, we need to add

$$\begin{pmatrix} \xi^3 \\ 0 \end{pmatrix}, \begin{pmatrix} 3\triangle y_j \xi^2 \eta \\ \triangle x_i \xi^3 \end{pmatrix}, \begin{pmatrix} \triangle y_j \xi \eta^2 \\ \triangle x_i \xi^2 \eta \end{pmatrix}, \begin{pmatrix} \triangle y_j \eta^3 \\ 3\triangle x_i \xi \eta^2 \end{pmatrix}, \begin{pmatrix} 0 \\ \eta^3 \end{pmatrix}. \tag{3.39}$$

3.5.5 Numerical results

Comparison of RKDG methods using curl-free P^k and standard P^k bases

In the following example, we consider a system under an external force $\mathbf{h}(x, y, t)$. The macroscale equations take the form of:

$$\begin{cases} \frac{\partial}{\partial t}\varepsilon - \nabla \mathbf{v} &= 0, \\ \rho_0 \frac{\partial}{\partial t}\mathbf{v} - \nabla \cdot P &= h_1(x, y, t), \\ \rho_0 \frac{\partial}{\partial t} e - \nabla \cdot (\mathbf{v}^T P) &= h_2(x, y, t). \end{cases} \tag{3.40}$$

We choose the source terms as

$$\begin{aligned} h_1(x, y, t) &= 0.01(\rho_0 - C_{11} - C_{12} - 2C_{44}) \cos(t + x + y), \\ h_2(x, y, t) &= 0.01^2(\rho_0 - C_{11} - C_{12} - 2C_{44}) \sin(2(t + x + y)). \end{aligned}$$

The initial conditions are given by,

$$\begin{cases} \varepsilon_{ij} &= 0.01 \sin(x + y) \\ v_i &= 0.01 \sin(x + y) \qquad\qquad i, j = 1, 2 \\ \rho_0 e &= E_0 + 0.01^2(C_{11} + C_{12} + 2C_{44}) \sin^2(x + y) \end{cases} \tag{3.41}$$

and with periodic boundary conditions the exact solutions are

$$\begin{cases} \varepsilon_{ij} &= 0.01 \sin(t + x + y) \\ v_i &= 0.01 \sin(t + x + y) \qquad\qquad i, j = 1, 2 \\ \rho_0 e &= E_0 + 0.01^2(C_{11} + C_{12} + 2C_{44}) \sin^2(t + x + y) \end{cases} \tag{3.42}$$

We use this set of exact solutions to test the accuracy and efficiency of the curl-free DG method comparing to the standard DG method. We list the L^2 errors and orders of accuracy using P^1 and P^2 DG methods in Tables 3.1, 3.2 and 3.3. The solutions are run to $T = 2\pi$. We can observe the optimal $(k+1)$-th order of accuracy both for the standard DG method and the curl-free DG method. The magnitudes of the errors for the same mesh are comparable for the two DG methods.

Table 3.1: L^2 error and order of accuracy for the stress strain ε

mesh	standard P^k		local curl-free P^k	
	L^2 error	order	L^2error	order
P^1				
10×10	2.12E-03	–	2.12E-03	–
20×20	5.28E-04	2.01	5.27E-04	2.00
40×40	1.31E-04	2.00	1.31E-04	2.00
80×80	3.32E-05	1.98	3.32E-05	1.98
160×160	8.35E-06	1.99	8.35E-06	1.99
P^2				
10×10	2.35E-03	–	1.92E-03	–
20×20	3.25E-04	2.86	2.62E-04	2.87
40×40	4.41E-05	2.88	3.39E-05	2.95
80×80	5.71E-06	2.95	4.33E-06	2.97
160×160	6.93E-07	3.04	5.47E-07	2.98

Thermal expansion

In this example, we study the effect of thermal expansion due to the temperature dependence of the stress. Initially the material is at rest with a homogeneous temperature distribution $T = 0.1$. Our computational domain is a square $[-1, 1] \times [-1, 1]$. We then increase the temperature in the middle $[-0.4, 0.4] \times [-0.4, 0.4]$ instantaneously to $T = 0.4$. This results in a thermal expansion that propagates outwards. We solve the macro equations (3.1) by the DG methods described above, and compare the results with those obtained with the two-dimensional central scheme [60].

Table 3.2: L^2 error and order of accuracy for the velocity

mesh	standard P^k		local curl-free P^k	
	L^2 error	order	L^2error	order
P^1				
10×10	2.29E-02	–	2.28E-03	–
20×20	7.88E-03	1.54	7.88E-03	1.53
40×40	1.96E-03	2.01	1.96E-03	2.01
80×80	4.70E-04	2.06	4.69E-04	2.06
160×160	1.14E-04	2.04	1.14E-04	2.04
P^2				
10×10	2.56E-03	–	2.49E-03	–
20×20	3.03E-04	3.08	2.95E-04	3.08
40×40	3.74E-05	3.02	3.68E-05	3.00
80×80	4.65E-06	3.01	4.63E-06	2.99
160×160	5.77E-07	3.01	5.82E-07	2.99

We present results in the following two cases: one is without the heat flux, the other is with the heat flux. Without the heat flux, the system is hyperbolic. Therefore it will have discontinuities in the solution under discontinuous initial conditions. In the presence of the heat flux, the system is parabolic. Therefore, the solution becomes smooth at $t > 0$ even if the initial condition is discontinuous. We will demonstrate the numerical results for the temperature distribution as well as the velocity field below.

The simplified constitutive model

We first run the simulation using the linear constitutive model (3.17) and (3.19) everywhere.

Without the heat flux: The results of the temperature distribution at $t = 0.01$ are shown in Fig. 3.3. The macro solver from left to right in Fig. 3.3 is the DG P^1, DG P^2 and the second-order central scheme, respectively. We can see that the DG scheme captures the shocks much better than the second-order central scheme using the same mesh. We can also see this from the cross section view of the two-

Table 3.3: L^2 error and order of accuracy for the energy

mesh	standard P^k		local curl-free P^k	
	L^2 error	order	L^2error	order
P^1				
10×10	3.38E-02	–	3.38E-02	–
20×20	7.97E-03	2.08	7.98E-03	2.08
40×40	7.42E-04	3.43	7.42E-04	3.43
80×80	1.75E-04	2.08	1.75E-04	2.08
160×160	4.42E-05	1.98	4.42E-05	1.98
P^2				
10×10	1.34E-01	–	1.12E-01	–
20×20	1.78E-02	2.91	1.54E-02	2.87
40×40	2.29E-03	2.96	1.99E-03	2.95
80×80	2.92E-04	2.97	2.54E-04	2.97
160×160	3.68E-05	2.99	3.21E-05	2.98

dimensional temperature distribution by the DG and the second-order central scheme in Fig. 3.4. Since we have not used any limiter for the results in the left picture of Fig. 3.4, there are some oscillations near the shocks. The application of limiters can eliminate these oscillations, see Fig. 3.4 right. For both figures, the shocks are sharper for the DG method than for the second-order central scheme.

With the heat flux: Adding the heat flux in our model is adding a diffusion term to the right side of PDEs. The LDG methods can easily deal with the diffusion term. The results of the temperature distribution using both DG P^1 and P^2 at $t = 0.01$ with a 80×80 mesh are shown in Fig. 3.5.

The full MD-based constitutive model

In this case, we compute the stress from MD in every cell. We first compute the temperature from the atomistic models. After the temperature is obtained, we compute the stress and energy flux from the atomistic model via a canonical ensemble.

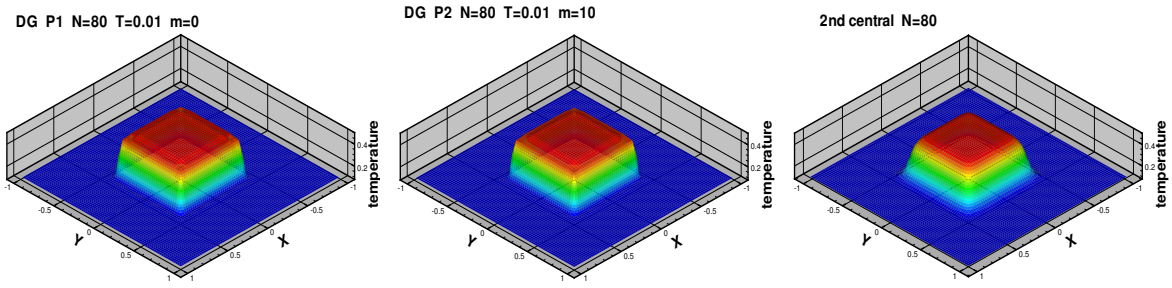

Figure 3.3: Temperature distribution without the heat flux (by the simplified constitutive model) at $t = 0.01$ with 80×80 cells. Left: DG P^1 with the TVD limiter; middle: DG P^2 with the TVB limiter $M = 10$; right: the second-order central scheme.

Without the heat flux. The results of the temperature distribution at $t = 0.01$ are shown in Fig. 3.6. We again compare our DG method with the second order central scheme. Using four times as many cells for the second-order central scheme as that for the DG P^1 method, we can still see the advantage of the DG method in capturing shocks. A clearer view in Fig. 3.7 shows the cross section of the two-dimensional temperature distribution computed by the DG P^1 and the second-order central scheme. The results of the velocity field at $t = 0.01$ are shown in Fig. 3.8. The direction of the velocity is pointing outward since the temperature is propagating outward.

With the heat flux. The results of the temperature distribution and the velocity field at $t = 0.01$ are shown in Fig. 3.9.

The domain decomposition model

Here we use the DDM procedure, as described in Sec. 3.5.3.

Without the heat flux: The results of the temperature distribution and the velocity fields using DG P^1 at $t = 0.01$ by the DDM model are shown in Fig. 3.10.

The results by the DDM are almost the same as the one we obtained by the full MD-based model (see Fig. 3.6 left and 3.8 left). This is more clearly seen from the

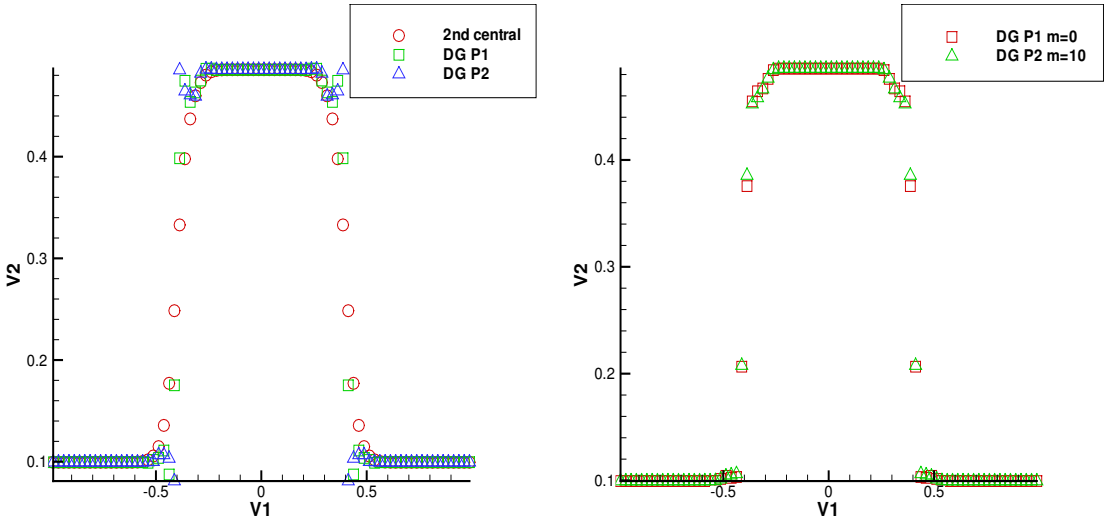

Figure 3.4: Cross section of the 2-D temperature distribution without the heat flux (by the simplified constitutive model) at $t = 0.01$ with 80×80 cells. Left: DG P^1, P^2 without limiters and the second-order central scheme; Right: DG P^1 with the TVD limiter and P^2 with the TVB limiter $M = 10$.

cross section of the two-dimensional temperature distribution by the DDM and the MD (see Fig. 3.13): they overlap almost completely.

The results of the temperature distribution and the velocity fields using the DG P^1 at $t = 0.03$ by the DDM model are shown in Fig. 3.11. As the time evolves, the heating is expanding outwards.

With the heat flux: The results of the temperature distribution and the velocity fields at $t = 0.01$ are shown in Fig. 3.12. Fig. 3.14 shows the results at $t = 0.03$. We can clearly see a thermal expansion propagating outwards.

The domain decomposition method (DDM) saves lots of computational cost. For example, we need 18 hours using 36 processors to evolve 1 time step with 30×30 cells for the MD DG P^1 method, while we only need less than 3 hours to do the same thing for the DDM. Actually, we only need to run the MD for the high temperature region in the middle. Initially, this part is only 16% of the whole domain. As time evolves, the high heat will propagate outwards and the area becomes even smaller.

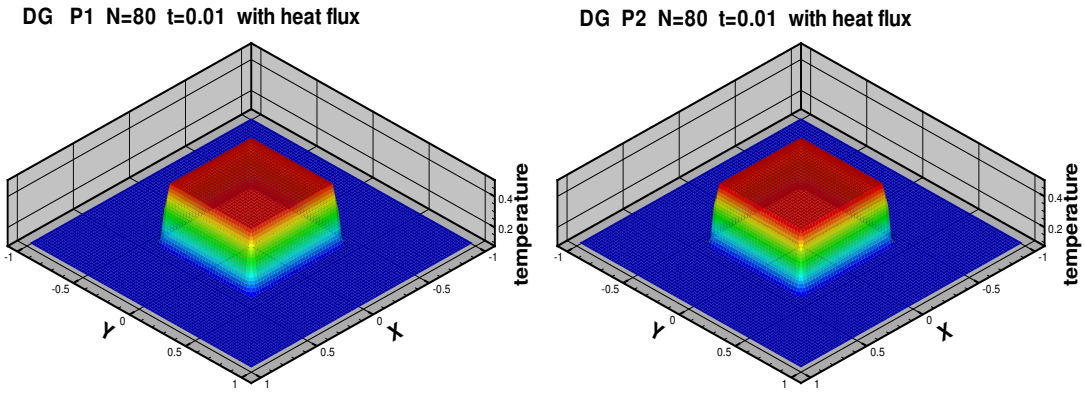

Figure 3.5: Temperature distribution with the heat flux (by the simplified constitutive model) at $t = 0.01$ with 80×80 cells. Left: DG P^1; right: DG P^2.

Wave propagation

As the last example, we simulate elastic wave propagation in a two dimensions unbounded medium. The experiment we present is described in [14]. The major difference is: their governing equations are based on linear elastodynamics, but ours are based on the domain decomposition model. We apply perfectly matched layers (PML) as described in [34] to simulate the propagation of waves in this open domain. See Appendix 3.7 for a brief description of the PML method.

Our computational domain is $\Omega = [-5, 5] \times [-5, 5]$ in two-dimensional, occupied by an elastic material, and we suppose that the initial condition (or the source) is supported in $D = [-3.5, 3.5] \times [-3.5, 3.5] \subset \Omega$. We are solving this elastodynamics problem with absorbing layers (PML) with width $\delta = 1.5$ on all four boundaries.

The initial data of the velocity and the stress are taken to be equal to zero. Initially, the material is of constant temperature $T = 0.167$ everywhere, and it is assumed to stay in the same temperature environment. An explosive source located at the point $(x_s, y_s) = (-3.15, 3.15)$ is introduced in the right side of the equations

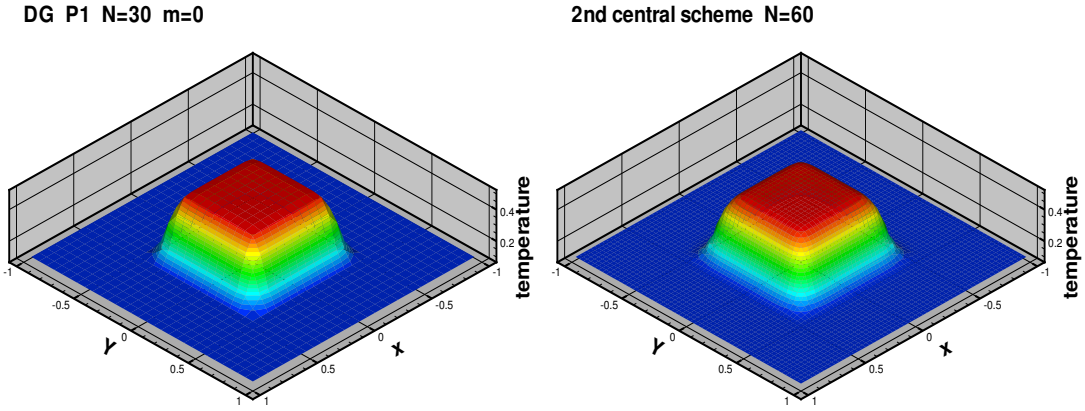

Figure 3.6: Temperature distribution without the heat flux (by the full MD-based model) at $t = 0.01$. Left: DG P^1 with 30×30 cells with the TVD limiter; right: the second-order central scheme with 60×60 cells.

of conservation of velocity,

$$f((x, y), t) = h(t)g(r)\vec{e}_r. \tag{3.43}$$

where $\vec{e}_r = (x - x_s, y - y_s)$, $r = ||\vec{e}_r||$. The function $h(t)$ is the so-called second-order Ricker signal with central frequency equal to $f_0 = 10Hz$ (see Fig. 3.15 left):

$$h(t) = [2\pi^2(f_0 t - 1)^2 - 1]e^{-\pi^2(f_0 t-1)^2}, \tag{3.44}$$

and the function $g(r)$ is the Gaussian function defined by (see Fig. 3.15 right)

$$g(r) = \frac{10e^{-7(r/r_0)^2}}{r_0^2}, \tag{3.45}$$

which is concentrated in a small disk of radius $r_0 = 0.3$.

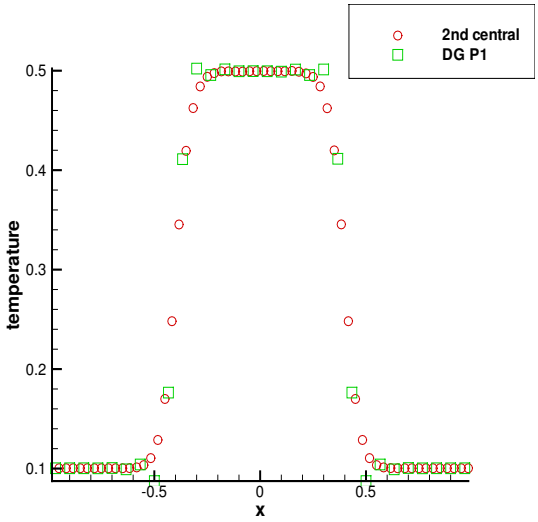

Figure 3.7: Cross section of the 2-D temperature distribution without the heat flux (by the full MD-based model) at $t = 0.01$. DG P^1 with 30×30 cells and the second-order central scheme with 60×60 cells.

The damping factor we use in the PML is as follows:

$$d(x) = \frac{3c}{2\delta^3} \log\left(\frac{1}{R}\right) x^2, \tag{3.46}$$

where $R = 10^{-3}$ is the theoretical reflection coefficient from the terminating reflection boundaries, i.e., the reflection coefficient is about 0.1%. c is an upper bound of the wave velocities, chosen as $c = 1$ here.

We show the snapshots of the velocity module using DG P^1 by the macro model in Fig. 3.16 and by the DDM model in Fig. 3.17. The PML works very well. The wave fronts are not circles because of the anisotropy of the medium. The waves are propagating outwards. At $t = 0.34$ (see Fig. 3.16, 3.17 upper right), some waves disappear in the upper left corner. The lower right waves are moving downwards as the time goes. At $t = 1.0$ (see Fig. 3.16, 3.17 bottom middle), these waves arrive at the lower right corner. At $t = 1.5$ (see Fig. 3.16, 3.17 bottom right), the amplitude of the velocity is already below 5×10^{-4}.

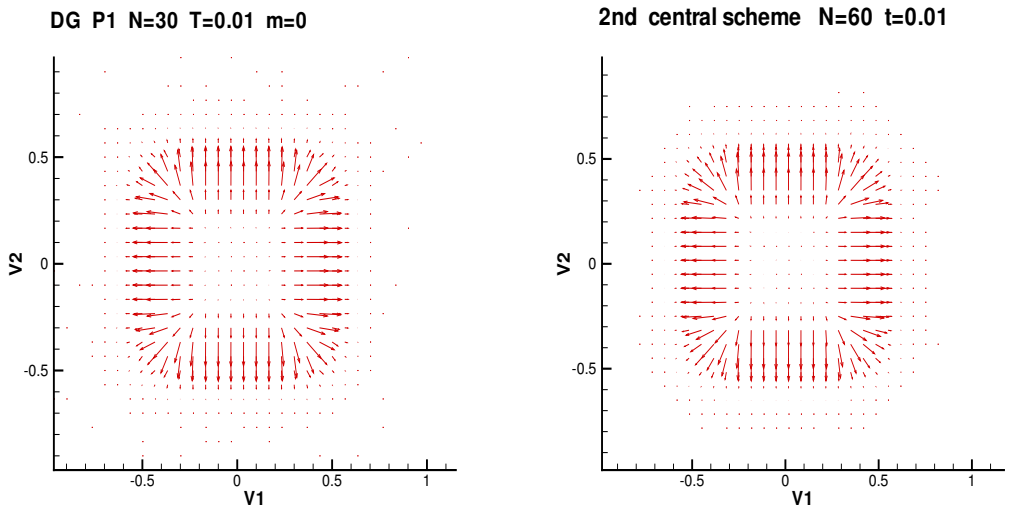

Figure 3.8: The velocity field without the heat flux (by the full MD-based model) at $t = 0.01$. Left: DG P^1 with 30×30 cells with the TVD limiter; right: the second-order central scheme with 60×60 cells.

3.6 Concluding remarks

We have developed a multiscale solver based on the DG method. The ability of the DG method to treat sharp wave fronts makes it particularly suitable for this problem. This has been demonstrated by a few test problems. More importantly it allows us to conveniently use atomistic models to provide constitutive data within the computation. The bottleneck of the method has been the atomistic component where MD is performed to calculate the elastic stress. This has been alleviated to some extent by first obtaining a simplified model in the case of small strain and low energy/temperature. More efficient methods are needed here to completely bypass MD. This is our current work in progress. Finally even though the numerical tests have been performed using rectangular elements, the DG methodology allows the use of arbitrary unstructured meshes with a full h-p adaptivity capability.

In the current framework, we have assumed that the material is a single perfect crystal. The next step is to model the dynamics of isolated defects, such as dislocations, phase boundaries, or crack tips. These problems bring up many interesting

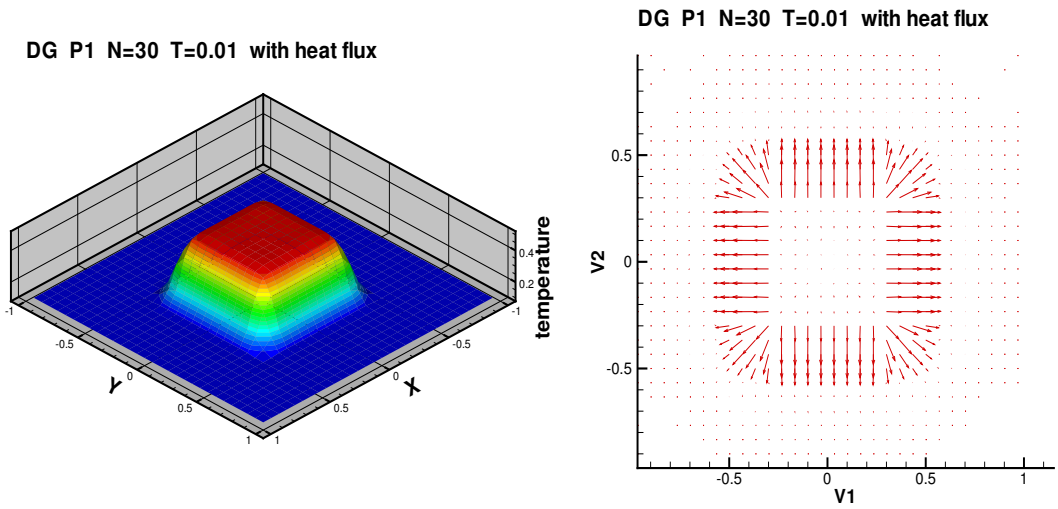

Figure 3.9: With the heat flux at $t = 0.01$. DG P^1 with 30×30 cells (by the full MD-based model). Left: the temperature distribution; right: the velocity field.

issues, such as the boundary conditions at the atomistic/continuum interface (e.g., see [54, 55]), adaptive mesh refinement, thermal fluctuations, etc. These issues will be addressed in future work.

3.7 Appendix: PML methods

The idea of the PML is to surround the computational domain with an absorbing layer (the PML region) such that the coupled system possesses the property of generating no reflection at the interface between the free medium and the artificial absorbing medium. The principle ideas of PML has been first introduced by Bérenger [15]. In [14], Bécache et al. have shown that it is possible to write in a systematic way of designing a PML model for a general first-order hyperbolic system. In this section, we will briefly describe the general construction.

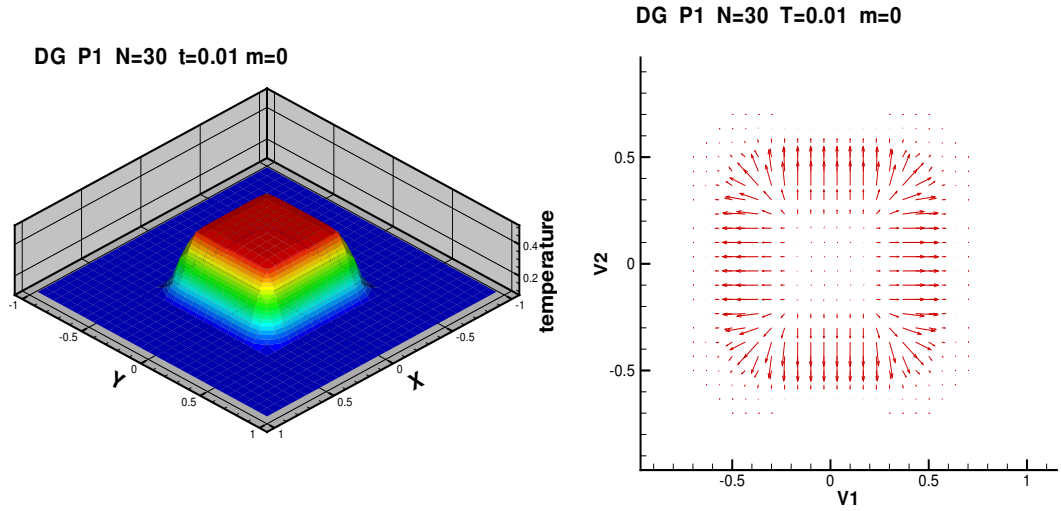

Figure 3.10: Without the heat flux at $t = 0.01$. DG P^1 with 30×30 cells (by the DDM). Left: the temperature distribution; right: the velocity field.

Consider a general two-dimensional first-order hyperbolic system

$$\begin{aligned} U_t + AU_x + BU_y &= 0, \\ U(t=0) &= U_0, \end{aligned} \tag{3.47}$$

where U is a $m-$vector, A and B are $m \times m$ matrices. To simplify the presentation, we assume our physical domain is in the left half plane i.e. $[x_1 < 0, x_2 = 0] \times [y_1, y_2]$. The initial condition U_0 is zero on the right half plane. The main idea of the PML model is to couple the equation in the left half-space with an equation in the right half-space such that there is no reflection at the interface $y = 0$.

The construction of the PML in the x-direction is to split $U = U^{(1)} + U^{(2)}$, such that the unknown $U^{(1)}$ is only associated to the derivatives with respect to x, and $U^{(2)}$ to the derivatives with respect to y. Then we introduce a damping factor $d(x)$

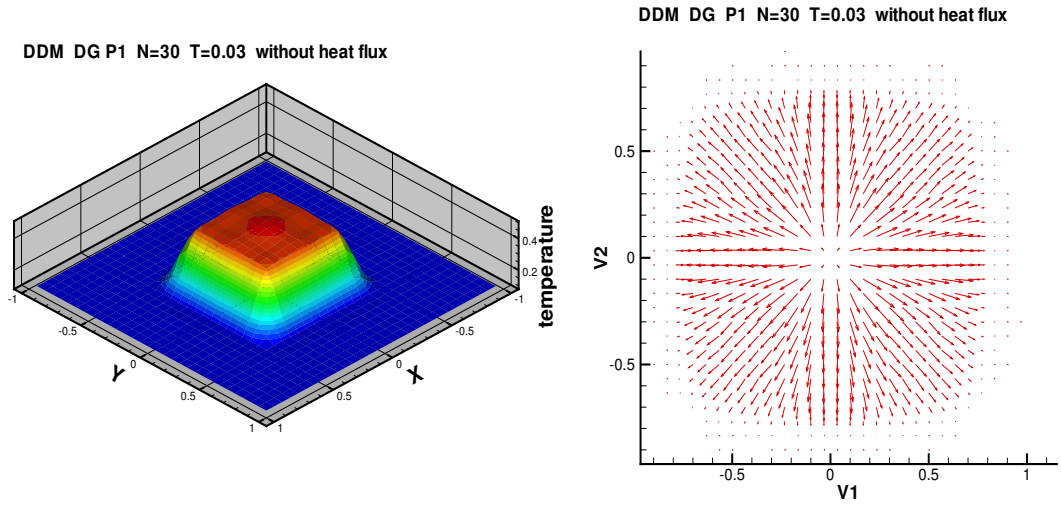

Figure 3.11: Without the heat flux at $t = 0.03$. DG P^1 with 30×30 cells (by the DDM). Left: the temperature distribution; right: the velocity field.

only on $U^{(1)}$. We obtain the system in the following:

$$\begin{aligned} U_t^{(1)} + d(x)U^{(1)} + AU_x &= 0, \\ U_t^{(2)} + BU_y &= 0, \\ U(t=0) &= U_0, \end{aligned} \tag{3.48}$$

where $d(x) = 0$ for $x < 0$, $d(x) \leq 0$, for $x \leq 0$. It is easy to see that U satisfies the same system of equations in the physical domain. The analysis [15] shows that there will be no reflection at the interface between the physical domain and the absorbing layers. Furthermore, the transmitted wave decreases exponentially during its propagation inside the layer.

In our example, the macroequations are a two-dimensional nonlinear system of parabolic equations. We will apply the PML to all the boundaries. So our macro

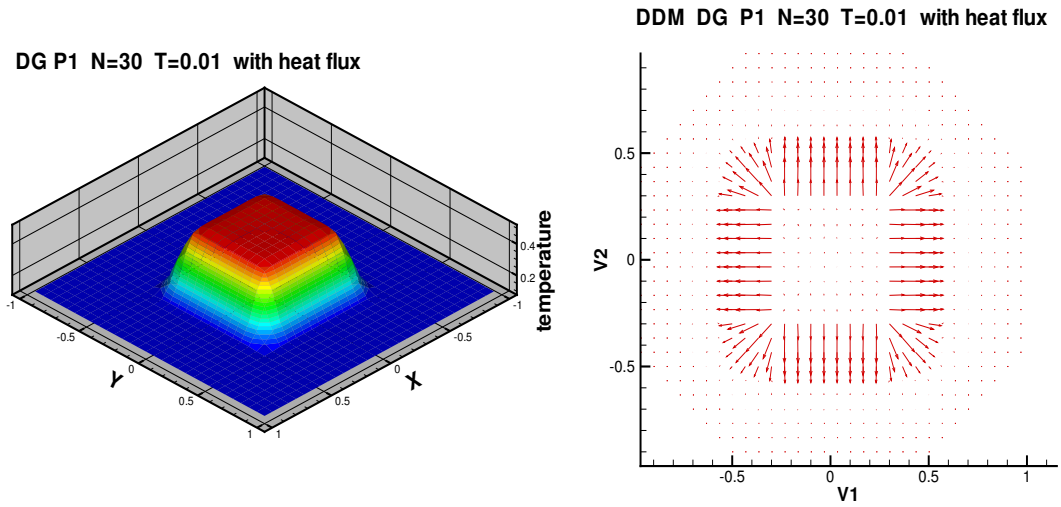

Figure 3.12: With the heat flux at $t = 0.01$. DG P^1 with 30×30 cells (by the DDM). Left: the temperature distribution; right: the velocity field.

equations can be rewritten in the following form:

$$\begin{aligned} U_t^{(1)} + d(x)U^{(1)} + F_x &= 0, \\ U_t^{(2)} + d(y)U^{(2)} + G_y &= 0, \\ U(t=0) &= U_0, \end{aligned} \tag{3.49}$$

where F and G are in (3.21), $d(x)$ and $d(y)$ are zeros in the physical domain and positive in the absorbing layers.

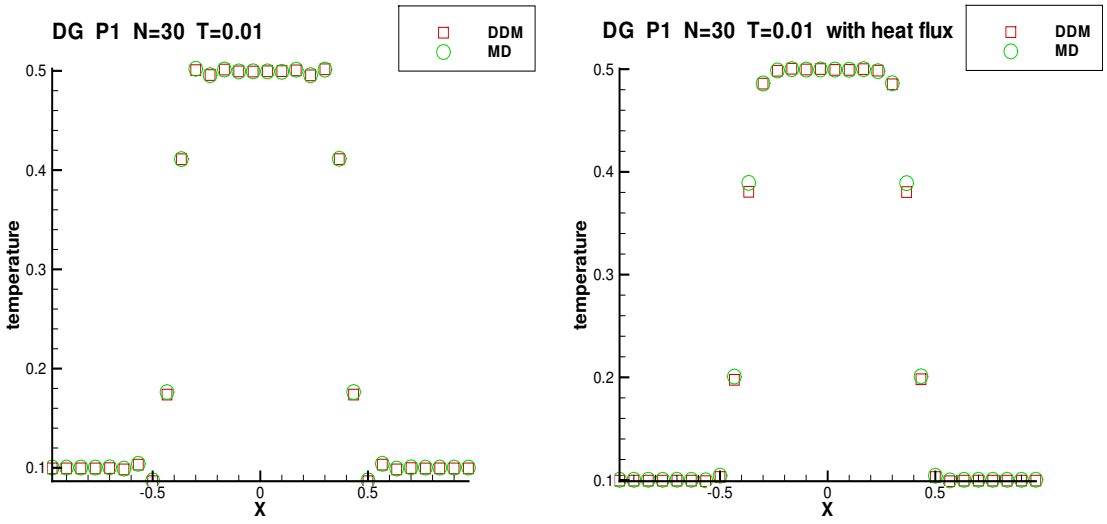

Figure 3.13: Comparison of DDM and full MD-based models: cross section of the 2-D temperature distribution at $t = 0.01$. DG P^1 with 30×30 cells. Left: without the heat flux; Right: with the heat flux.

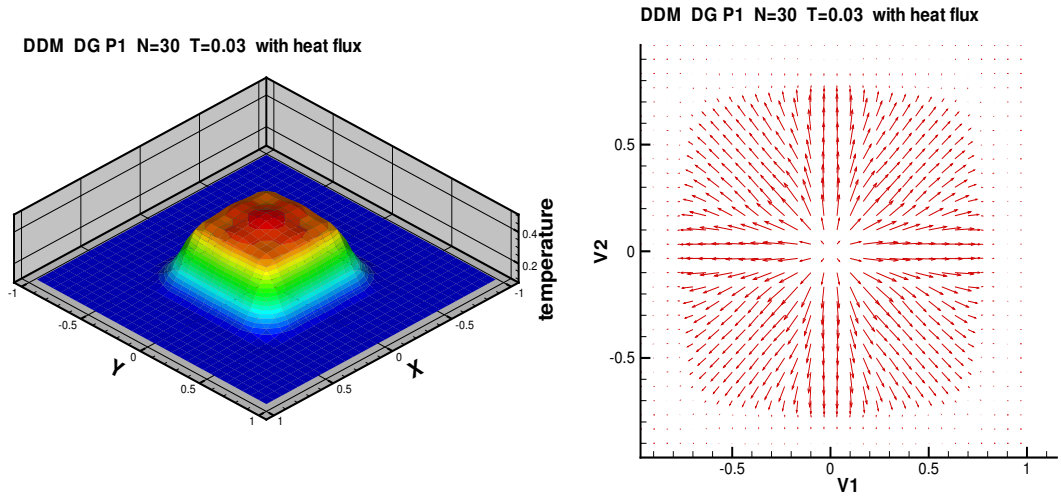

Figure 3.14: With the heat flux at $t = 0.03$. DG P^1 with 30×30 cells (by the DDM). Left: the temperature distribution; right: the velocity field.

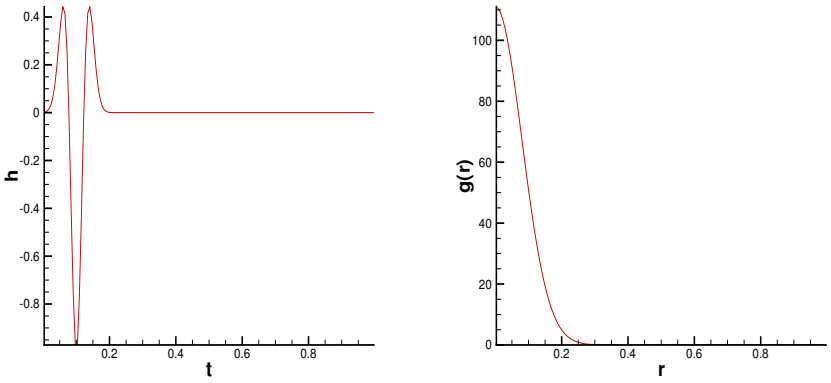

Figure 3.15: Left: the Ricker signal $h(t)$; right: the Gaussian function $g(r)$.

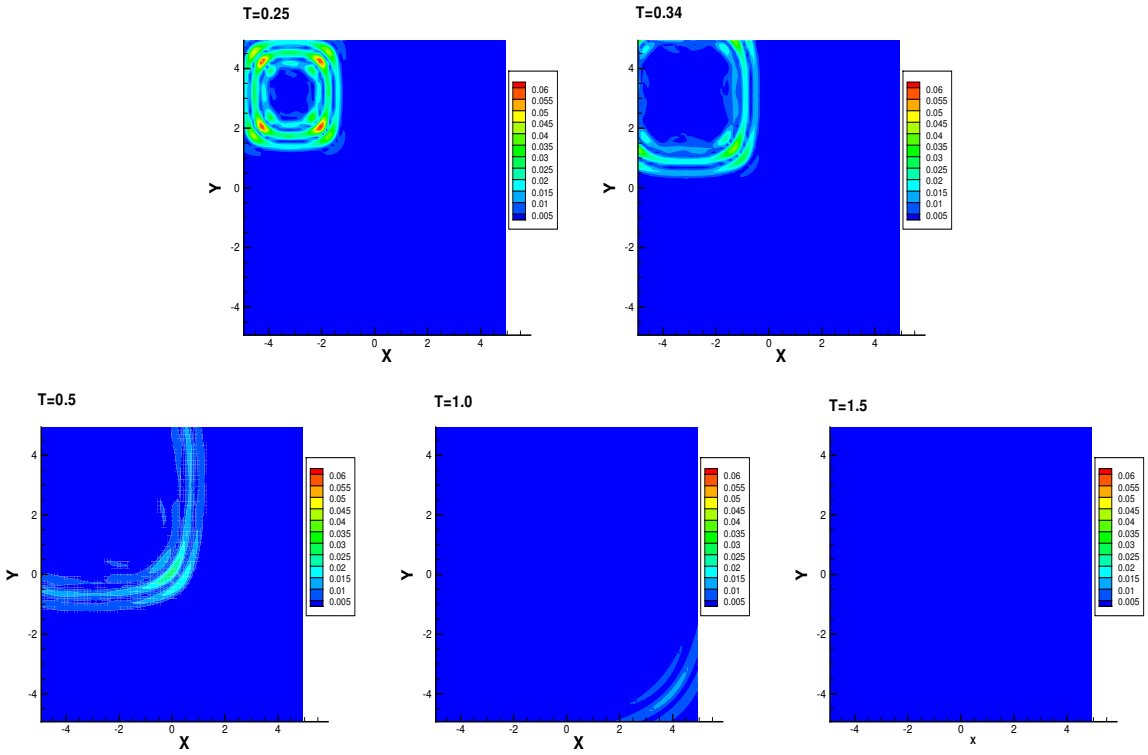

Figure 3.16: Snapshots of the velocity module at different times (by the simplified constitutive model): DG P^1 with 80×80 cells.

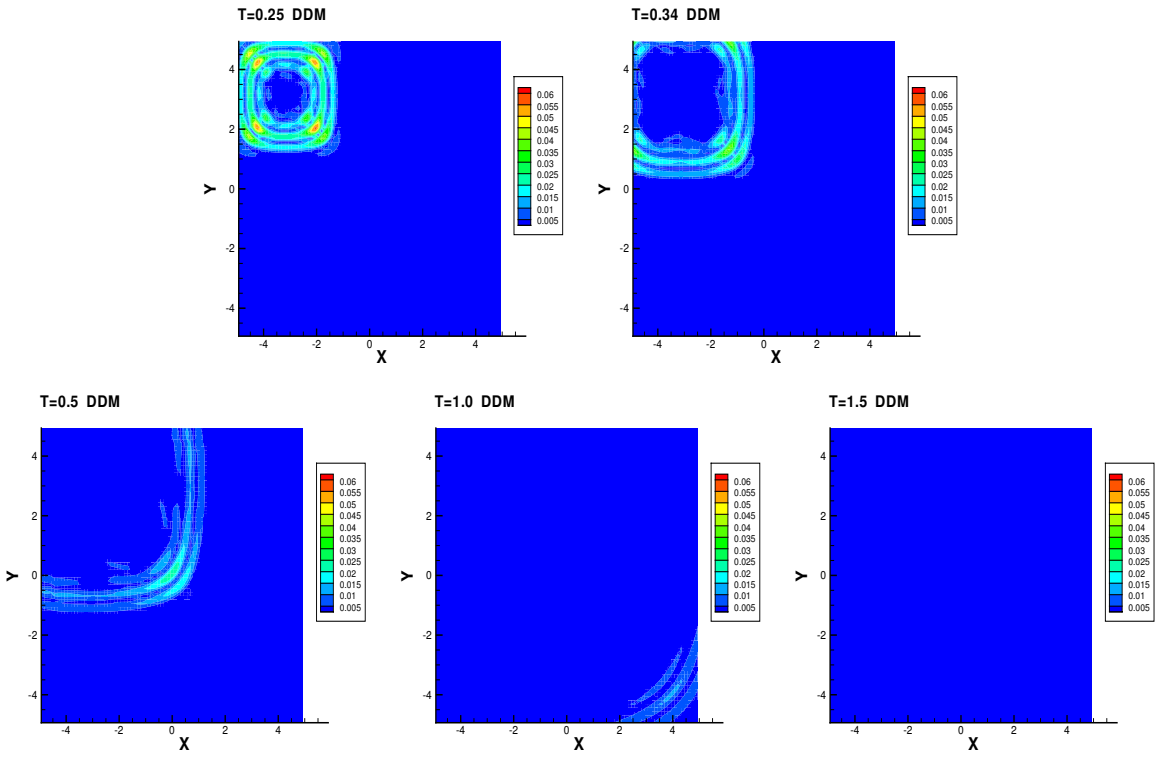

Figure 3.17: Snapshots of the velocity module at different times (by the DDM model): DG P^1 with 80×80 cells.

Chapter 4

The WKB Local Discontinuous Galerkin Method for the Simulation of Schrödinger Equation in a Resonant Tunneling Diode

4.1 Introduction

In recent studies of nanoscale semiconductor structures, quantum effects arise and have to be taken into account in the modeling by means of the Schrödinger equation. There are computational difficulties in solving the Schrödinger equations. On one hand, the oscillatory behavior of the solutions requires a refined spacial grid. On the other hand, a large number of Schrödinger equations need to be solved in order to simulate an electronic device. For example, in the resonant tunneling diode (RTD) [4, 63, 3], only the electrons having an energy extremely close to the resonant energy are transmitted from the source to the drain. To collect the resonances, there are

thousands of Schrödinger equations to solve.

In [3], Ben Abdallah and Pinaud have proposed a WKB approach using traditional continuous finite element method for the one-dimensional model. They obtain an explicit formula for the phase factor of wave functions from WKB asymptotics [16] and then use this phase factor to interpolate the nodal values of the wave function. Therefore, a much coarser grid is allowed comparing with the method based on polynomials. A convergence analysis for this method is presented in [58]. In [2], this method is generalized to a special two-dimensional device in which the two-dimensional Schrödinger equation is approximated by a one-dimensional non-diagonal Schrödinger system [64] for which a WKB type approach can be derived (see [59]). One limitation of the method in these works is, however, that it is difficult to generalize it to two-dimensional devices for which the two-dimensional Schrödinger equation cannot be easily converted to one-dimensional systems and must be solved in two-dimensional elements, as it is very difficult to have continuity at the element interface with such multiscale basis functions in two dimensions.

Comparing with traditional continuous finite element Galerkin methodology, the advantage of the DG and LDG methods includes their flexibility in h-p adaptivity and their allowance of complete discontinuity at element interfaces. It is computationally advantageous to combine the WKB approach with the LDG method, which is the main purpose of this chapter: we present a WKB-LDG method to solve the Schrödinger equation, which is in essence an LDG method based on exponential basis functions in the spirit of [74]. The method maintains the advantages of the general DG/LDG methods and saves in computational cost as well as memory when compared with the regular polynomial-based LDG methods. To conveniently compare our results to those obtained with the traditional continuous finite element WKB method, we mostly consider the same examples as in [3]. The results in this chapter are only one-dimensional, however it is feasible to extend the WKB-LDG method to two-dimensional devices, because there is no continuity requirement for the solution

across element interfaces. The extension to two-dimensional devices does involve the non-trivial task of constructing suitable multiscale basis functions, which involves an accurate estimate of the local oscillation direction and is left for future work. We remark that, in recent years, there have been many contributions in developing DG methods for solving PDEs in semi-conductor device simulations, such as those in [22, 23, 56, 57]. Comparing with these earlier works, our work is the first example of using the DG method to solve the RTD model with the Schrödinger equation and also the first time exponential approximation spaces are appeared in the DG method for solving the Schrödinger equation.

4.1.1 The Schrödinger-Poisson problem

We consider the RTD model (see [3]) on the interval $[a, b]$ with $a < a_1 < a_2 < a_3 < b_3 < b_2 < b_1 < b$ along the growth direction x. Its conduction band profile consists of two barriers of height v_1 located at $[a_2, a_3]$ and $[b_3, b_2]$. A bias energy $\triangle v$ is applied between the source ($x < a_1$) and the collector ($x > b_1$) regions. The regions $[a, a_1]$ and $[b_1, b]$ are highly doped with doping density n_d^1, and $[a_1, a_2]$ and $[b_2, b_1]$ are doped with n_d^2. The transport is assumed to be ballistic and one-dimensional. The wave function of the electrons injected at $x = a$ with momentum $p > 0$ satisfies a stationary effective-mass Schrödinger equation with open boundary conditions [1]:

$$\begin{cases} -\frac{\hbar^2}{2m}\varphi_p'' - qV\varphi_p = E_p^a\varphi_p, \ (p \geq 0) \\ \hbar\varphi_p'(a) + ip\varphi_p(a) = 2ip; \quad \hbar\varphi_p'(b) = ip_b\varphi_p(b), \end{cases} \tag{4.1}$$

where m is the effective mass (assumed to be constant in the device), q is the elementary positive charge of the electron, V is the total electrostatic potential in the device and

$$p_b = \sqrt{p^2 + 2qm(V_b - V_a)}, \quad E_p^a = \frac{p^2}{2m} - qV_a.$$

Similarly, the wave function of electrons injected at $x = b$ with momentum $p \leq 0$ satisfies the equation:

$$\begin{cases} -\frac{\hbar^2}{2m}\varphi_p'' - qV\varphi_p = E_p^b\varphi_p, \ (p < 0) \\ \hbar\varphi_p'(b) + ip\varphi_p(b) = 2ip; \quad -\hbar\varphi_p'(a) = ip_a\varphi_p(a), \end{cases} \tag{4.2}$$

where

$$p_a = \sqrt{p^2 + 2qm(V_a - V_b)}, \quad E_p^b = \frac{p^2}{2m} - qV_b.$$

The transmission coefficients are defined by

$$T(p) = \frac{\sqrt{(p^2 + 2qm(V_b - V_a))^+}}{|p|}|\varphi_p(b)|^2 \quad \text{for } p \geq 0, \tag{4.3}$$

$$T(p) = \frac{\sqrt{(p^2 - 2qm(V_b - V_a))^+}}{|p|}|\varphi_p(a)|^2 \quad \text{for } p < 0, \tag{4.4}$$

where $(a)^+ = \max(a, 0)$.

The electrons are assumed to be in a mixed state so that the electronic density is given by

$$n(x) = \int_{-\infty}^{\infty} g(p)|\varphi_p(x)|^2 dp, \tag{4.5}$$

where $g(p) := g_a(p)$ for $p \geq 0$ and $g(p) := g_b(p)$ for $p < 0$. g_a and g_b are the statistics of the electrons injected at $x = a$ and $x = b$ respectively. In our case, $g(p)$ is a Fermi-Dirac integral given by

$$g(p) = \frac{mk_bT}{2\pi^2\hbar^3}\log\left(1 + \exp\left(\left(-\frac{p^2}{2m} + E_F\right)/k_bT\right)\right), \tag{4.6}$$

where E_F is the Fermi energy defined implicitly by the neutrality condition for the doping density in the source and drain regions (see [4]):

$$n_d^1 = \int_{-\infty}^{\infty} g(p)dp. \tag{4.7}$$

The current density is given by

$$J = \frac{q}{m}\int_{-\infty}^{\infty} g(p)pT(p)dp. \tag{4.8}$$

The electrostatic potential $V = V_e + V_s$. V_e is the external potential including double barriers and applied bias and V_s is the self-consistent potential modeling the electron-electron interaction

$$\begin{cases} V_s''(x) = \frac{q}{\epsilon}(n(x) - n_D(x)) \\ V_s(a) = V_s(b) = 0 \end{cases}, \tag{4.9}$$

where ϵ is the dielectric constant and n_D is the doping density.

Since the equations (4.1), (4.2), (4.5) and (4.9) are coupled together, the Gummel method [42] is used to accelerate the iterating speed (see [63]). We solve

$$\frac{d^2V_s^{new}}{dx^2} = \frac{q}{\epsilon}\left[n(V_s^{old})\exp\left((V_s^{new} - V_s^{old})/V_{ref}\right) - n_D\right] \tag{4.10}$$

instead of Eq. (4.9), where the potential reference V_{ref} is adjusted to decrease the number of iterations. The linear version of the Gummel method is given by

$$\frac{d^2V_s^{new}}{dx^2} = \frac{q}{\epsilon}\left[n(V_s^{old})\left(1 + \frac{(V_s^{new} - V_s^{old})}{V_{ref}}\right) - n_D\right]. \tag{4.11}$$

When no bias is applied, the Gummel method converges with zero as an initial guess for the self-consistent potential. When the bias is not zero, the obtained potential from the no-bias case is used to initialize the algorithm.

4.1.2 The WKB approach

In [3], the authors have presented a WKB scheme using the continuous finite element method. The motivation of their basis construction comes from the WKB

asymptotics [16], i.e. for $E + qV(x) > 0$ and when $\hbar \to 0$,

$$\varphi(x) \sim \frac{A}{\sqrt[4]{2m(E+qV(x))}} e^{iS(x)} + \frac{B}{\sqrt[4]{2m(E+qV(x))}} e^{-iS(x)}, \tag{4.12}$$

where A and B are constants, $S(x)$ is the dimensionless action,

$$S(x) = \frac{\sqrt{2m}}{\hbar} \int_{x_0}^{x} \sqrt{E + qV(s)} ds \tag{4.13}$$

and x_0 is an integration constant. Therefore, their WKB-interpolated function in the continuous finite element case for the cell I_j is given by

$$\widetilde{\varphi}(x) = \frac{A_j}{\sqrt[4]{2m(E+qV(x))}} e^{iS(x)} + \frac{B_j}{\sqrt[4]{2m(E+qV(x))}} e^{-iS(x)}, \quad x \in I_j. \tag{4.14}$$

The constants A_j and B_j are determined by the nodal values at the cell boundaries.

We will introduce a similar idea but based on the LDG methodology, which is called the WKB-LDG method in next section.

4.2 Numerical methods

In this section, we are going to first introduce the regular LDG solver for the Schrödinger equations (4.1) and (4.2) and then define the WKB-LDG method. We will use the same notations as in Chap. 2.

4.2.1 Traditional LDG methods for the Schrödinger equations

For simplicity, we first write the stationary Schrödinger equation (4.1) as follows

$$\begin{cases} -\varphi_p'' - a(x)\varphi_p = 0, \ (p \geq 0) \\ \hbar\varphi_p'(a) + ip\varphi_p(a) = 2ip; \ \hbar\varphi_p'(b) = ip_b\varphi_p(b), \end{cases} \tag{4.15}$$

where

$$a(x) = \frac{2m}{\hbar^2}(qV + E_p^a).$$

Since the equation is linear, we can first solve for $\tilde{\varphi}_p$ on a boundary condition $\tilde{\varphi}_p(a) = 1$ and $\tilde{\varphi}_p'(b) = ip_b\tilde{\varphi}_p(b)$ and then normalize $\tilde{\varphi}_p$ by $2ip/[\hbar u_p'(a) + ipu_p(a)]$ to recover φ_p (see [63]).

Therefore, we apply the LDG method on the PDE

$$\begin{cases} -u'' - a(x)u = 0, \\ u(a) = 1;\ u'(b) = c_b u(b), \end{cases} \tag{4.16}$$

where $c_b = ip_b/\hbar$ is a constant for fixed p. Notice that we have used u to denote $\tilde{\varphi}_p$.

The numerical fluxes $\widehat{u_h}$ and $\widehat{q_h}$ are chosen to be the alternate fluxes: $\widehat{u_h} = u_h^-$ and $\widehat{q_h} = q_h^+$. At the two boundary points, $\widehat{u_h}_{\frac{1}{2}} = u(a)$ and $\widehat{q_h}_{N+\frac{1}{2}} = c_b(u_h)^-_{N+\frac{1}{2}}$. In this one-dimensional case, this LDG scheme is guaranteed to give an optimal convergence rate of h^{k+1} in the L^2-norm for both u and q.

Similarly, we can solve the Schrödinger equation with $p < 0$. We solve the following PDE for u first, then normalize it by $2ip/[\hbar u_p'(b) + ipu_p(b)]$:

$$\begin{cases} -u'' - a(x)u = 0, \\ u(b) = 1;\ u'(a) = c_a u(a), \end{cases} \tag{4.17}$$

where $c_a = -ip_a/\hbar$. Since the boundary conditions are opposite to the $p > 0$ case, the numerical fluxes should also be opposite, i.e. we take $\widehat{u_h} = u_h^+$ and $\widehat{q_h} = q_h^-$. At the two boundary points, $\widehat{u_h}_{N+\frac{1}{2}} = u(b)$ and $\widehat{q_h}_{\frac{1}{2}} = c_a(u_h)^+_{\frac{1}{2}}$.

4.2.2 The WKB-LDG scheme

The WKB-LDG scheme is a WKB scheme based on the LDG method. More precisely, if we consider a "constant form" of the WKB asymptotics, the finite element space

for our WKB-LDG method is

$$E^2(\alpha) = \{v_h : (v_h)|_{I_j} \in \text{span}\{1, e^{i\alpha_j(x-x_j)}, e^{-i\alpha_j(x-x_j)}\}, \quad j = 1, \ldots, N\}, \tag{4.18}$$

where

$$\alpha_j = \frac{\sqrt{2m}}{\hbar}\sqrt{E + qV(x_j)}, \quad j = 1, \ldots, N. \tag{4.19}$$

The approximation space $E^2(\alpha)$ is actually an exponential space. In [74], the authors have proved the L^2 stability and error estimates of the DG method based on non-polynomial approximation spaces including exponential spaces for time-dependent PDEs. The similar proof can also be obtained for stationary problems. In particular, $E^2(\alpha)$ has a third order approximation convergence rate. The proof is simple: we write

$$\begin{pmatrix} 1 \\ e^{i\alpha_j(x-x_j)} \\ e^{-i\alpha_j(x-x_j)} \end{pmatrix} = \begin{pmatrix} 1 & 0 & 0 \\ 1 & i\alpha_j & -\frac{\alpha_j^2}{2} \\ 1 & -i\alpha_j & -\frac{\alpha_j^2}{2} \end{pmatrix} \begin{pmatrix} 1 \\ (x-x_j) \\ (x-x_j)^2 \end{pmatrix} + \begin{pmatrix} 0 \\ -\frac{i\alpha_j^3}{3!} \\ \frac{i\alpha_j^3}{3!} \end{pmatrix} (x-x_j)^3 + O((\triangle x_j)^4).$$

for $x \in I_j$, and denote

$$A = \begin{pmatrix} 1 & 0 & 0 \\ 1 & i\alpha_j & -\frac{\alpha_j^2}{2} \\ 1 & -i\alpha_j & -\frac{\alpha_j^2}{2} \end{pmatrix}, \quad b = \begin{pmatrix} 0 \\ -\frac{i\alpha_j^3}{3!} \\ \frac{i\alpha_j^3}{3!} \end{pmatrix}. \tag{4.20}$$

It is easy to verify that A is invertible and A and b are independent of $\triangle x_j$. By Prop. 3.1 in [74], $E^2(\alpha)$ is a third order approximation space. Therefore, even when the solution of the PDE is not close to the asymptotic functions in this approximation

space, we should still obtain comparable accuracy to the regular polynomial-based DG method using the same number of degrees of freedom.

As a simple example, we assume V is constant and solve the simple PDE

$$\begin{cases} -u'' - 4u = 0, \quad x \in [0, 2\pi], \\ u(0) = 0; \ u'(2\pi) = 2. \end{cases} \tag{4.21}$$

The exact solution for this problem is $u = \sin(2x)$. The numerical results obtained by the WKB-LDG method using the space $E^2(\alpha)$ with different values of α, and the regular polynomial-based DG method, are shown in Table 4.1. If we choose $\alpha = 2$ which corresponds to the correct asymptotic value, we can obtain basically the round-off error (in quadruple precision). If, however, we choose a different value for α, either smaller ($\alpha = 1$), or bigger ($\alpha = 3$), we will not have any advantage over the regular, polynomial-based LDG method, as the exact solution is not closer to $E^2(\alpha)$ than to $P^2(I_j)$. However, even in these cases we still obtain the expected third order convergence and the error levels for the same mesh are comparable with that of the regular, polynomial-based LDG method.

Table 4.1: L^2 errors and orders of accuracy for the WKB-LDG method using the space $E^2(\alpha)$ with different values of α, and the regular polynomial-based DG method

N	L^2 error	L^2 error	Order	L^2 error	Order	L^2 error	Order
	$\alpha = 2$	$\alpha = 1$		$\alpha = 3$		LDG P^2	
10	4.42E-29	1.31E-2	–	2.38E-2	–	1.73E-2	–
20	6.30E-27	1.61E-3	3.03	2.71E-3	3.14	2.15E-3	3.01
40	1.45E-25	2.01E-4	3.00	3.36E-4	3.01	2.68E-4	3.00
80	1.56E-23	2.51E-5	3.00	4.19E-5	3.00	3.35E-5	3.00
160	1.33E-21	3.14E-6	3.00	5.24E-6	3.00	4.19E-6	3.00

If we would like to have higher order convergence, we can consider the higher

order exponential space

$$\begin{aligned} E^4(\alpha) &= \{v_h : (v_h)|_{I_j} \in \text{span}\{1, e^{i\alpha_j(x-x_j)}, e^{-i\alpha_j(x-x_j)}, \\ &\quad e^{i\alpha_j(x-x_j)}(x-x_j), e^{-i\alpha_j(x-x_j)}(x-x_j)\}, \quad j = 1, \ldots, N\}, \end{aligned} \tag{4.22}$$

and so on.

Remark 4.1. To make sure the basis functions are well defined, it is necessary to require that α_j is not a multiple of π, otherwise the basis functions will be linearly dependent. This is the so-called non-resonance condition (see [3]). Typically, the point x_j satisfying $\alpha_j = 0$ (i.e. $|E + qV(x_j)| = 0$) is called a turning point. In this case, we define a threshold $\delta > 0$. When $|E + qV(x_j)| \geq \delta$, the space $E^2(\alpha)$ will be used; when $|E + qV(x_j)| < \delta$, we simply use $E^2(\alpha_0)$, where $\alpha_0 = \frac{\sqrt{2m}}{\hbar}\sqrt{\delta}$.

4.3 Numerical results

In this section, we demonstrate our WKB-LDG method by some numerical simulations of the RTD model. First, we concentrate on the WKB-LDG scheme for the linear Schrödinger equations. By 'linear', we mean that we solve the Schrödinger equation (4.1) only without coupling it to the equations for density and self-consistent potential. The energy and total potential are given in advance. Here the total potential is precomputed by a reference solution which is obtained using the regular, polynomial-based LDG P^2 method with 1350 cells. Next, our WKB-LDG scheme is tested on fully nonlinear problems. It will couple the integration (4.5) for the density and the Poisson potential equation (4.11) for the self-consistent potential.

In all the numerical simulations, we use the same parameters as those used in [3], see Table 4.2. As mentioned before, the reference solution is obtained with the regular, polynomial-based LDG P^2 method with 1350 cells.

Table 4.2: RTD parameters

a	a_1	a_2	a_3	b_3	b_2	b_1	b	m_{eff}	V_1
0 nm	50 nm	60 nm	65 nm	70 nm	75 nm	85 nm	135 nm	$0.067m_e$	-0.3V

4.3.1 The Schrödinger equation

In this section, we concentrate on the efficiency and accuracy of the WKB-LDG scheme for the linear Schrödinger equation. First, we test our WKB-LDG scheme on a simple case where the exact solutions are available. Next, we will add a non-zero potential bias and consider the self-consistent potential in the simulation, which will introduce turning points.

A simple case

If there is no bias applied to the RTD model and we do not consider the self-consistent potential, the total potential V is piecewise constant and the Schrödinger equation has an analytical solution. Therefore it is easy to use this simple case to test the accuracy of the schemes. We use the same examples as those in [3]. One example has the energy very close to the double-barrier first resonant energy $E_p^a = 0.0895eV$ and the other has the energy far from this value $E_p^a = 0.046072eV$. The total potential $V = V_e$,

$$V_e(x) = \begin{cases} 0, & x < a_2 \\ V_1, & a_2 < x < a_3 \\ 0, & a_3 < x < b_3 \\ V_1, & b_3 < x < b_2 \\ 0, & b_2 < x \end{cases} . \tag{4.23}$$

We solve the linear Schrödinger equation (4.1) under these two energies. The errors are listed in Table 4.3. We list the results of the WKB-LDG scheme with 13 cells and

with 23 cells. The mesh with 13 cells contains 2 cells each in $[a, a_1]$, $[a_1, a_2]$, $[a_2, a_3]$, $[b_3, b_2]$, $[b_2, b_1]$, $[b_1, b]$, and one cell in $[a_3, b_3]$. The mesh with 23 cells contains 6 cells each in $[a, a_1]$, $[b_1, b]$, 2 cells each in $[a_1, a_2]$, $[b_2, b_1]$,$[a_2, a_3]$ and $[b_3, b_2]$, and 3 cells each in $[a_3, b_3]$. We can see that the WKB-LDG method presents only a round-off error in the linear case. As a comparison, the polynomial-based LDG P^1 method has a second order convergence and the LDG P^2 method has a third order convergence. Notice that LDG P^2 with 1350 cells has a comparable accuracy as the WKB-LDG method. That is the reason we choose the LDG P^2 with 1350 cells to produce the reference solution in all the simulations in this work.

We can also see the perfect match between the WKB-LDG solution and the exact solution from the figures. Fig. 4.1 shows the wave function modulus at the resonant energy $E_p^a = 0.0895eV$ and Fig. 4.2 shows the case of an non-resonant energy $E_p^a = 0.046072eV$. Both of the figures use a WKB mesh of 13 cells.

Table 4.3: Results in the linear case with exact solution

	N	L^2 error	N	L^2 error
	$E = 0.0895eV$		$E = 0.046072eV$	
WKB-LDG	13	4.63E-14	13	1.57E-16
	23	2.63E-12	23	6.78E-16
LDG P^1	135	2.66E-4	135	2.00E-5
	1350	1.76E-6	1350	1.84E-7
LDG P^2	135	6.00E-6	135	4.90E-7
	1350	6.13E-9	1350	4.94E-10

A case with turning points

We add a bias of $0.08V$ at the edges of the device and a precomputed self-consistent potential into the Schrödinger equation (4.1). This time we do not have an analytical solution any more, hence we use a reference solution obtained with the polynomial-based LDG P^2 method of 1350 cells. In the case of turning points, we use a threshold of $\delta = 0.001eV$.

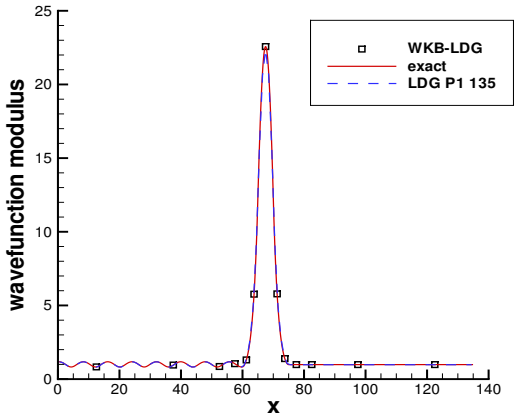

Figure 4.1: Comparison among the exact solution, the WKB-LDG solution and the LDG P^1 solution: resonant case with $E = 0.0895eV$. 13 cells are used in the WKB-LDG method. 135 cells are used in the LDG P^1 method.

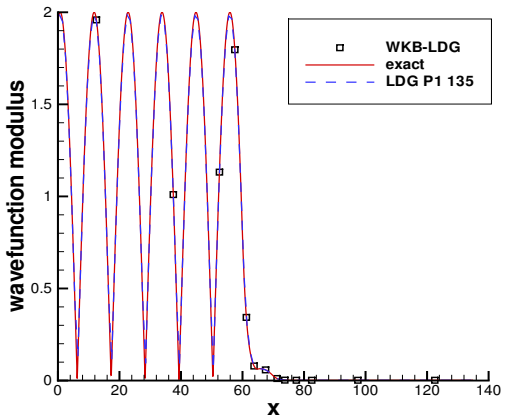

Figure 4.2: Comparison among the exact solution, the WKB-LDG solution and the LDG P^1 solution: non-resonant case with $E = 0.046072eV$. 13 cells are used in the WKB-LDG method. 135 cells are used in the LDG P^1 method.

We consider 4 different energies, a very low energy $E = 0.0039eV$, a low energy $E = 0.059eV$, a higher energy $E = 0.17eV$ and a very high energy $E = 1.11eV$. The errors are listed in Table 4.4. We only test the WKB-LDG scheme with 23 cells this time. The errors of the WKB-LDG method with 23 cells and the LDG P^2 method with 135 cells have similar magnitude of errors. That is, the WKB-LDG method uses only 17% of the cells used by the LDG P^2 method and much less computational time to reach the same resolution.

Table 4.4: Results in the linear case with turning points

	N	L^2 error	N	L^2 error
	$E = 0.0039eV$		$E = 0.17eV$	
WKB-LDG	23	1.42E-4	23	5.96E-5
LDG P^2	135	2.07E-5	135	6.92E-6
	$E = 0.059eV$		$E = 1.11eV$	
WKB-LDG	23	2.69E-4	23	4.56E-5
LDG P^2	135	1.80E-5	135	5.23E-5

We also show the figures of the wave function modulus at the energy $E = 0.0039eV$, $E = 0.059eV$, $E = 0.17eV$ and $E = 1.11eV$ in Figures 4.3, 4.4, 4.5 and 4.6 respectively. All of them are using a mesh size of 23 cells. We can see that the WKB-LDG solutions overlap very well with the lines of the reference solutions. Especially, in Figures 4.3 and 4.4, we plot the WKB-LDG solution completely as a function, not just a sample point in each cell, and we can see that the WKB-LDG solution reproduces the reference solution very well.

4.3.2 The fully non-linear problem

In this section, the WKB-LDG scheme is illustrated on the fully non-linear RTD model. The electronic density is computed using (4.5) with an integration between $-k_{\max}$ and $k_{\max}$, where $k = \sqrt{2mE}/\hbar$ is used instead of the energy E (see [3]). We use the trapezoidal rule (which is spectrally accurate for compactly supported

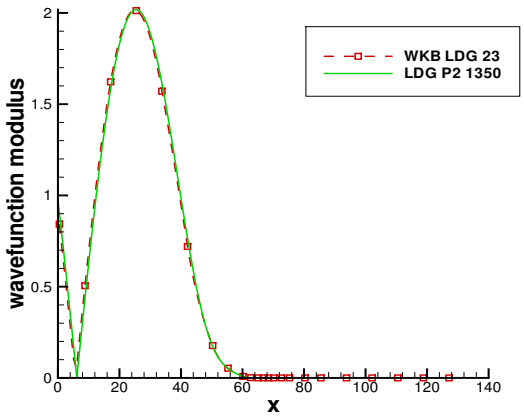

Figure 4.3: Comparison between the reference solution and the WKB-LDG solution: $E = 0.0039eV$. 23 cells are used in the WKB-LDG method. In each cell, the WKB-LDG solution is plotted as a function using 9 points.

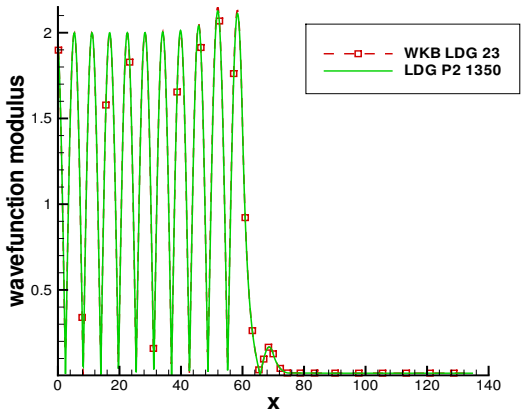

Figure 4.4: Comparison between the reference solution and the WKB-LDG solution: $E = 0.17eV$. 23 cells are used in the WKB-LDG method. In each cell, the WKB-LDG solution is plotted as a function using 27 points.

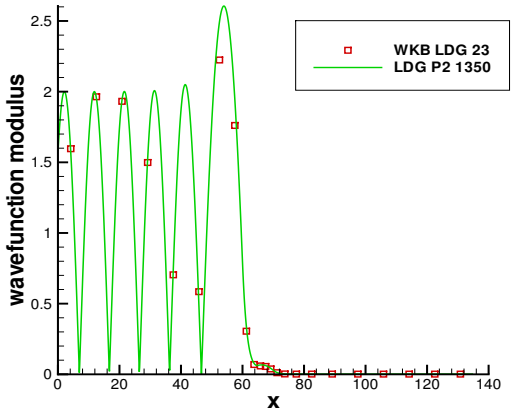

Figure 4.5: Comparison between the reference solution and the WKB-LDG solution: $E = 0.059eV$. 23 cells are used in the WKB-LDG method.

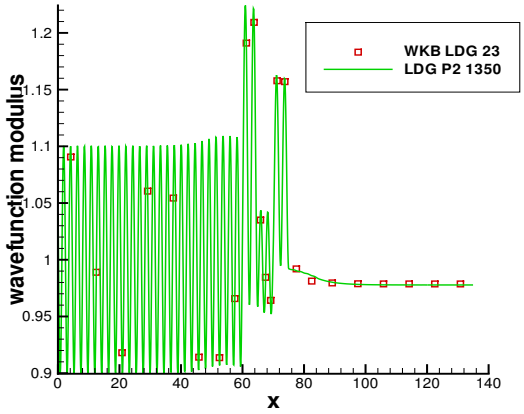

Figure 4.6: Comparison between the reference solution and the WKB-LDG solution: $E = 1.11eV$. 23 cells are used in the WKB-LDG method.

analytical functions) to evaluate the integral and take a mesh size $\triangle k$ for the integral. The self-consistent potential is computed using the Gummel iteration described in Section 4.1.1. The parameters we use are listed in Table 4.5.

Table 4.5: Parameters used for the density and the self-consistent potential computation

T	n_d^1	n_d^2	$k_{\max}$	$\triangle k$	V_{ref}	ε_r
$300K$	$10^{18}cm^{-3}$	$10^{15}cm^{-3}$	$0.0626\mathring{A}^{-1}$	$5 \times 10^{-5}\mathring{A}^{-1}$	$0.03V$	11.44

We still use the polynomial-based LDG P^2 method with 1350 cells to produce a reference solution and use the same 23 cells for the WKB-LDG method. In [3], it is remarked that a WKB mesh with these few cells might be too coarse for computing the density and the self-consistent potential, and an interpolation could be used to obtain a finer mesh for the purpose of density or self-consistent potential computation. Our numerical results using the WKB-LDG method turn out to be very good if we use the same 23 cells throughout the simulation. Therefore, we have kept the same mesh for the wave function computation as well as for the computation of the density and the self-consistent potential.

Table 4.6 lists the errors of the density in both the zero bias case and the $0.08eV$ bias case. We can see that the WKB-LDG method gives a pretty good result here. Also it saves around 70% computational time comparing to similar results obtained by the regular polynomial-based LDG method.

Table 4.6: Results in the fully non-linear problem: L^2 errors of density and CPU time (seconds/iteration).

	N	L^2 error	CPU time	L^2 error	CPU time
	bias=$0eV$			bias=$0.08eV$	
WKB-LDG	23	3.57E-4	2.43	9.72E-4	2.53
LDG P^2	135	1.15E-4	10.29	1.15E-4	10.38

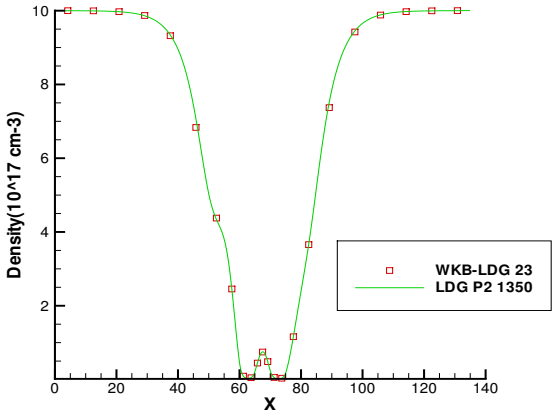

Figure 4.7: Comparison between the reference solution and the WKB-LDG solution: density for the full non-linear case. 23 cells are used in the WKB-LDG method.

We present the figures of the density and the self-consistent potential under $0.08eV$ bias in Fig. 4.7 and Fig. 4.8. The WKB-LDG results and the reference solutions overlap very well.

An important curve, the I-V curve, is the function of current in (4.8) versus the applied voltage bias. The obtained curve is shown in Fig. 4.9. The results obtained by the WKB-LDG method with 23 cells are almost indistinguishable from the reference results. For the purpose of verification, we also compare our reference solution with the reference solution reported in Fig. 20 of [3], see Fig. 4.10. We observe that the two reference solutions overlap well. By comparing Fig. 4.9 with Fig. 20 of [3], we conclude that our WKB-LDG method with 23 cells produces a solution which is much closer to the reference solution than the continuous finite element WKB result with 34 points.

4.4 Concluding remarks

In this chapter, we have developed a multiscale LDG solver for the semiconductor RTD model. The main ingredient of this scheme is the WKB-LDG method for solving

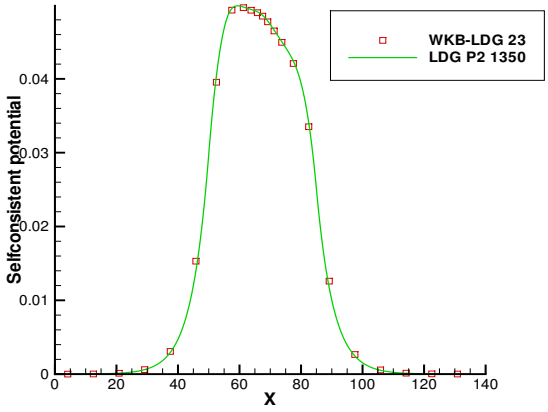

Figure 4.8: Comparison between the reference solution and the WKB-LDG solution: self-consistent potential for the full non-linear case. 23 cells are used in the WKB-LDG method.

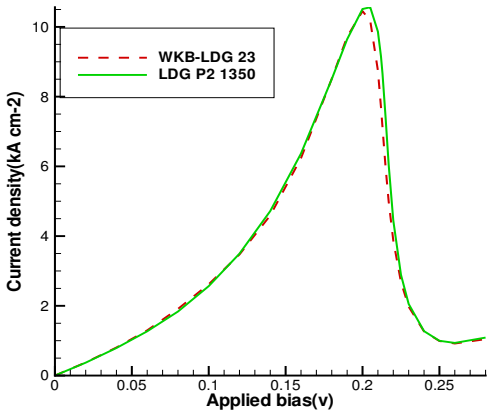

Figure 4.9: Comparison between the reference solution and the WKB-LDG solution: the I-V characteristics of a resonant tunneling diode. 23 cells are used in the WKB-LDG method.

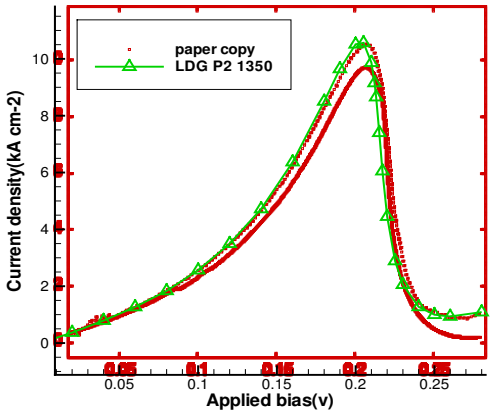

Figure 4.10: Comparison between the reference solution used in this work and that used in Fig. 20 of [3]: the I-V characteristics of a resonant tunneling diode. Solid line with triangle: the reference solution used in this work; dashed line: the reference solution in Fig. 20 of [3]; thicker solid line: the continuous finite element WKB result with 34 points in Fig. 20 of [3].

the Schrödinger equations. Numerical experiments indicate that the WKB-LDG solver has excellent accuracy on very coarse meshes. Comparing with the continuous finite element based WKB method in [3], the WKB-LDG method allows the full usage of the potential of this methodology in easy h-p adaptivity and feasibility for the extension to two-dimensional case. In future work, we will generalize our WKB-LDG method to two-dimensional devices, starting from those with a strong fixed directional dependence such as the double gate MOSFETs in [2], and then moving on to further explore this method to fully two-dimensional problems with changing and eventually no privileged direction.

Chapter 5

The Multiscale Discontinuous Galerkin Method for Solving a Class of Second Order Elliptic Problems with Rough Coefficients

5.1 Introduction

In this chapter we consider the second order elliptic boundary value problems

$$-\nabla \cdot (A^\varepsilon(\mathbf{x})\nabla u) = f(\mathbf{x}) \quad \text{in } \Omega \tag{5.1}$$

with boundary condition

$$u = 0 \quad \text{on } \partial\Omega,$$

where Ω is a rectangular domain and f is a function in $L^2(\Omega)$.

Specifically, $A^\varepsilon(\mathbf{x}) = a^\varepsilon(x)$ in 1-D problems and $A^\varepsilon(\mathbf{x}) = \begin{pmatrix} a^\varepsilon(x) & 0 \\ 0 & b^\varepsilon(y) \end{pmatrix}$ in 2-D problems. $a^\varepsilon(x)$ and $b^\varepsilon(y)$ are oscillatory functions involving a small scale ε.

We assume that

$$0 < \beta \leq a^{\varepsilon}(x), b^{\varepsilon}(y) \leq \alpha < \infty \tag{5.2}$$

for any $(x, y) \in \Omega$, where α and β are constants.

For simplicity, we will first consider the 1-D problem on the domain $\Omega = [0, 1]$

$$\begin{aligned} &-(a^{\varepsilon}(x)u_x)_x = f(x), \quad 0 < x < 1, \\ &u(0) = u(1) = 0. \end{aligned} \tag{5.3}$$

If the coefficient $a^{\varepsilon}(x)$ is rough, then the solution u to (5.3) will also be rough; to be specific, u will not in general be in $H^2([0, 1])$ and may not be in $H^{1+\varepsilon}([0, 1])$ for any $\varepsilon > 0$.

In [12, 11], Babuška and Osborn proposed an approach to this kind of problems based on continuous finite element methods. Theoretical proofs were provided for both 1-D and 2-D cases and numerical experiments were presented in the 1-D case. In [75], Yuan and Shu applied the approach of Babuška and Osborn to the Babuška-Zlámal DG method [13]. They developed a multiscale Babuška-Zlámal DG method based on a non-polynomial basis (see [74]) for (5.3). Both theoretical proofs and numerical tests were presented for the 1-D case. We mention that u is in $H^2([0, 1])$ in the proofs in [75]. In this chapter, we are going to prove the same stability and error estimate but assume u is only in $H^1([0, 1])$. Furthermore, we will generalize this approach to an 'LDG method'. The main difficulty here is due to the two spaces of u_h and q_h (see Chap. 2). We remark that for the uniqueness of the numerical solution, the approximation space for u_h is not the same as the approximation space for q_h. The test function space is not even the same as the approximation space. Therefore, the method is a local discontinuous Petrov-Galerkin (LDPG) method.

5.2 Multiscale approximation spaces

In our DG method, we will use the spaces constructed below to approximate the solution to (5.3) (see [75]):

$$S^k = \{\phi \in H^1(0,1) : -(a^\varepsilon(x)\phi_x)_x|_{I_j} \in P^{k-2}(I_j) \text{ for each } j\}. \tag{5.4}$$

Here we define $P^{-1}(I_j) = \{0\}$.

The multiscale approximation space (5.4) for our model problem (5.3) is explicitly given by

$$S^k = \left\{ v : v|_{I_j} \in \text{span}\left\{ 1, \int_{x_j}^x \frac{1}{a^\varepsilon(\xi)}d\xi, \int_{x_j}^x \frac{\xi - x_j}{a^\varepsilon(\xi)}d\xi, ..., \int_{x_j}^x \frac{(\xi - x_j)^{k-1}}{a^\varepsilon(\xi)}d\xi \right\} \right\}. \tag{5.5}$$

We have some properties of the spaces S^k (see Lemma 4.1 in [12]).

Lemma 5.1. Given a function $u \in H^1([0,1])$, there is a unique interpolation u_I satisfying

$$\begin{aligned} &u_I \in S^k, \\ &u_I(x_{j+\frac{1}{2}}) = u(x_{j+\frac{1}{2}}), \quad j = 0, 1, \ldots, n, \\ &\textstyle\int_{I_j}(u - u_I)(x - x_{j-\frac{1}{2}})^l dx = 0, \quad l = 0, \ldots, k-2, \ , j = 1, \ldots, n. \end{aligned} \tag{5.6}$$

Then we have the approximation results (see Lemma 4.3 in [12]) as:

Lemma 5.2.

$$\|u - u_I\|_{0,[0,1]} \leq C(\alpha, \beta)h^{k+1}\|f\|_{k-1,[0,1]}, \tag{5.7}$$

$$\|u - u_I\|_{1,[0,1]} \leq C(\alpha, \beta)h^{k}\|f\|_{k-1,[0,1]}, \tag{5.8}$$

where $C(\alpha, \beta)$ is independent of u but depends on α, β.

Thoughout this chapter, we will use the notations for the norms and seminorms

in the following:

$$\|u\|^2_{k,[0,1]} = \int_{[0,1]} \sum_{|\alpha|\le k} |D^\alpha u|^2,$$

$$|u|^2_{k,[0,1]} = \int_{[0,1]} \sum_{|\alpha|= k} |D^\alpha u|^2.$$

Remark 5.1. There are other ways of proofs in which we do not need to impose the continuity on the cell boundary and are able to get the same optimal approximation results as in Lemma 5.2, see [75].

5.2.1 Multiscale LDPG method

We first review the standard LDG scheme for problem (5.3).

We rewrite the Eq. (5.3) as a first order system

$$q - u_x = 0, \quad -(a^\varepsilon q)_x = f. \tag{5.9}$$

Then the general formulation of the MD-LDG method for the elliptic problem (5.3) is to find $u_h, q_h \in V_h^k$ such that

$$\int_{I_j} q_h w_h dx + \int_{I_j} u_h (w_h)_x dx - \widehat{u_h}_{j+\frac{1}{2}} (w_h)^-_{j+\frac{1}{2}} + \widehat{u_h}_{j-\frac{1}{2}} (w_h)^+_{j-\frac{1}{2}} = 0 \tag{5.10}$$

$$\int_{I_j} a^\varepsilon q_h (v_h)_x dx - \widehat{a^\varepsilon q_h}_{j+\frac{1}{2}} (v_h)^-_{j+\frac{1}{2}} + \widehat{a^\varepsilon q_h}_{j-\frac{1}{2}} (v_h)^+_{j-\frac{1}{2}} = 0 \tag{5.11}$$

for all test functions $v_h, w_h \in V_h^k$ with the flux choice (2.26) or (2.27).

Instead of using $V_h^k = P^k$ in the standard MD-LDG method, we use the multiscale approximation space (5.5) for u_h. The motivation of choosing the basis for q_h is straightforward: q_h is the approximation of u_x. Therefore, we take the derivatives of the basis functions in (5.5) and get the approximation space for q_h, i.e.

$$S_q^k = \left\{ v : v|_{I_j} \in \text{span}\left\{ \frac{1}{a^\varepsilon(x)}, \frac{x - x_j}{a^\varepsilon(x)}, \ldots, \frac{(x-x_j)^{k-1}}{a^\varepsilon(x)} \right\} \right\}. \tag{5.12}$$

Having determined the multiscale approximation spaces for u_h and q_h, we are now in a position to choose the test function spaces. The motivation of determining the test function spaces is from the analysis of the uniqueness of the solution. There exists only one zero solution to the problem (5.3) when $f = 0$. If we take $w_h = a^\varepsilon q_h$ and $v_h = u_h$ in (5.10) and (5.11) and add them together, then we will obtain

$$\int_{I_j} a^\varepsilon(x) q_h^2 dx = 0. \tag{5.13}$$

This can be a way to prove the uniqueness of the problem. Therefore it is natural to choose w_h in the same space as $a^\varepsilon q_h$, and v_h in the same space as u_h. Notice that, $a^\varepsilon q_h$ is actually a polynomial. Then our multiscale method now becomes: to find $u_h \in S^k$, $a^\varepsilon q_h \in P^k$ such that (5.10) and (5.11) hold for all test functions $v_h \in S^k$, $w_h \in P^k$. Since the test functions are not in the same spaces as the approximation functions, this is a multiscale LDPG method.

5.3 Results

In this section, we generalize the proof for the multiscale Babuška-Zlámal DG method in [75] to the $u \in H^1([0,1])$ case. The primal formulation of the Babuška-Zlámal DG method is to find $u_h \in V_h^k$ such that

$$\sum_{j=1}^{N} \int_{I_j} a^\varepsilon(x)(u_h)_x(v_h)_x dx + \sum_{j=0}^{N} a^\varepsilon(x_{j+\frac{1}{2}}) \frac{\eta}{h} [u_h]_{j+\frac{1}{2}} [v_h]_{j+\frac{1}{2}} = \sum_{j=1}^{N} \int_{I_j} f v_h dx$$

for all test functions $v_h \in V_h^k$, where $\eta \approx O(\triangle x^{-2k})$ and $[u] = u^+ - u^-$. We denote the primal form $B_h(u_h, v_h)$ as the left-hand-side of the primal formulation. First we will discuss the boundedness and the stability of B_h under some appropriate norm, then we will give the error estimate for the multiscale Babuška-Zlámal DG method.

Define a new seminorm

$$|v|^2_{L,\Omega} := \int_\Omega a^\varepsilon |(a^\varepsilon v_x)_x|^2 dx, \tag{5.14}$$

and a new space

$$H^L(\Omega) := \{v \in H^1(\Omega), |v|_{L,\Omega} < \infty\}$$

with the norm

$$\|v\|^2_{L,\Omega} = \|v\|^2_{1,\Omega} + |v|^2_{L,\Omega}. \tag{5.15}$$

This is the key point of our work. Although the solution u is not in $H^2([0,1])$, it is in this new H^L space. We will follow the lines of the proofs in [75] but under this new H^L norm.

To consider the boundedness and stability of the primal form B_h, we let $V(h) := S^k + H^L(\Omega) \cap H^1_0(\Omega)$ and define the following seminorms and norms for $v \in V(h)$:

$$|v|^2_{1,h} = \sum_{j=1}^N |v|^2_{1,I_j}, \quad \text{where } |v|^2_{1,I_j} = \int_{I_j} |v_x|^2 dx,$$

$$|v|^2_* = \sum_{j=0}^N h^{-(2k+1)} [v]^2_{j+\frac{1}{2}}, \tag{5.16}$$

$$|||v|||^2 := |v|_{1,h} + |v|^2_*. \tag{5.17}$$

Lemma 5.3. (Boundedness) There exists some constant C_b such that

$$B_h(w,v) \le C_b \,|||\, w \,|||\, |||v\,||| \quad \forall w, v \in V(h). \tag{5.18}$$

Proof. From the Babuška-Zlámal DG method, we have

$$B_h(w,v) = \sum_{j=1}^N \int_{I_j} a^\varepsilon(x) w_x v_x dx + \sum_{j=0}^N a^\varepsilon(x_{j+\frac{1}{2}}) \frac{\eta}{h} [w]_{j+\frac{1}{2}} [v]_{j+\frac{1}{2}}. \tag{5.19}$$

We can easily obtain

$$\sum_{j=1}^{N} \int_{I_j} a^{\varepsilon}(x) w_x v_x dx \leq C(\alpha) |w|_{1,h} |v|_{1,h}, \tag{5.20}$$

and

$$\sum_{j=0}^{N} a^{\varepsilon}(x_{j+\frac{1}{2}}) \frac{\eta}{h} [w]_{j+\frac{1}{2}} [v]_{j+\frac{1}{2}} \leq C(\alpha)(\sup \eta) h^{2k} |w|_* |v|_*. \tag{5.21}$$

where C is a constant only depending on α and $\sup \eta = O(h^{-2k})$. Combining (5.20) and (5.21), the proof is completed. □

Lemma 5.4. (Stability) There exists some constant C_s such that

$$B_h(v, v) \geq C_s \| \mid v \mid \|^2 \quad \forall v \in V(h). \tag{5.22}$$

Proof. We have

$$B_h(v, v) = \sum_{j=1}^{N} \int_{I_j} a^{\varepsilon}(x) v_x v_x dx + \sum_{j=0}^{N} a^{\varepsilon}(x_{j+\frac{1}{2}}) \frac{\eta}{h} [v]_{j+\frac{1}{2}} [v]_{j+\frac{1}{2}}. \tag{5.23}$$

It's easy to see

$$\sum_{j=1}^{N} \int_{I_j} a^{\varepsilon}(x) v_x v_x dx \geq C(\beta) |v|_{1,h}^2, \tag{5.24}$$

and

$$\sum_{j=0}^{N} a^{\varepsilon}(x_{j+\frac{1}{2}}) \frac{\eta}{h} [v]_{j+\frac{1}{2}}^2 \geq C(\beta)(\inf \eta) h^{2k} |v|_*^2, \tag{5.25}$$

where C is a constant only depending on β and we need $\inf \eta = O(h^{-2k})$. Therefore, we prove the stability. □

Lemma 5.5. (Approximation) Let $u(x)$ be the exact solution of (5.3). There exists some interpolant $u_I \in S^k (k \geq 1)$ such that

$$\| \mid u - u_I \mid \| \leq C h^k \| f \|_{k-1,\Omega}. \tag{5.26}$$

Proof. We choose u_I to be the interpolant (5.6), then the jumps of $u - u_I$ will vanish on the boundaries. We have

$$|||u - u_I||| = |u - u_I|_{1,\Omega} \leq \|u - u_I\|_{1,\Omega} \leq Ch^k \|f\|_{k-1,\Omega}. \tag{5.27}$$

□

Lemma 5.6. (Regularity) For each $f \in L^2(\Omega)$, the solution u of (5.3) is in $H_0^1(\Omega) \cap H^L(\Omega)$. Furthermore, there is a constant $C = C(\alpha, \beta)$, depending on α and β but independent of f, such that

$$\|u\|_{L,\Omega} \leq C(\alpha, \beta)\|f\|_{0,\Omega}. \tag{5.28}$$

Proof. The proof here mainly follows the lines in [11].

Let u be the unique solution to (5.3) in $H_0^1(\Omega)$. We introduce the change of variables or mapping

$$\tilde{x}(x) = \int_0^x \frac{ds}{a(s)}, \tag{5.29}$$

and the notation

$$\tilde{u}(\tilde{x}(x)) = u(x), \quad x \in \Omega. \tag{5.30}$$

The mapping maps the domain $\Omega = [0, 1]$ onto $\tilde{\Omega} = \left(0, \int_0^1 \frac{ds}{a(s)}\right)$. We see that $\tilde{u} \in H^2(\Omega)$ if and only if $u \in H^1(\Omega), a^\varepsilon u_x \in H^1(\Omega)$, which is equivalent to $u \in H^L(\Omega)$. The new PDE is

$$\begin{cases} -\tilde{u}_{\tilde{x}\tilde{x}} = \widetilde{a^\varepsilon} \tilde{f} & \text{in } \tilde{\Omega}, \\ \tilde{u} = 0 & \text{on } \partial\tilde{\Omega}. \end{cases} \tag{5.31}$$

As a consequence of Bernstein Theorem, (5.31) is uniquely solvable in $H_0^1(\tilde{\Omega}) \cap H^2(\tilde{\Omega})$, and

$$\|\tilde{u}\|_{2,\tilde{\Omega}} \leq C(\alpha, \beta)\|\widetilde{a^\varepsilon} \tilde{f}\|_{0,\tilde{\Omega}}. \tag{5.32}$$

$$\begin{aligned}
\|u\|^2_{L,\Omega} &= \int_\Omega u^2 dx + \int_\Omega u_x^2 dx + \int_\Omega a^\varepsilon |(a^\varepsilon u_x)_x|^2 dx \\
&= \int_{\tilde{\Omega}} \widetilde{a^\varepsilon} \tilde{u}^2 d\tilde{x} + \int_{\tilde{\Omega}} \tfrac{1}{a^\varepsilon} |\tilde{u}_{\tilde{x}}|^2 d\tilde{x} + \int_{\tilde{\Omega}} |\tilde{u}_{\tilde{x}\tilde{x}}|^2 d\tilde{x} \\
&\leq \max(\alpha, \tfrac{1}{\beta}, 1) \|\tilde{u}\|^2_{2,\tilde{\Omega}} \\
&\leq \max(\alpha, \tfrac{1}{\beta}, 1) C(\alpha,\beta)^2 \|\widetilde{a^\varepsilon} \tilde{f}\|^2_{0,\tilde{\Omega}} \\
&\leq \alpha^2 \max(\alpha, \tfrac{1}{\beta}, 1) C(\alpha,\beta)^2 \|f\|^2_{0,\Omega}.
\end{aligned} \tag{5.33}$$

□

Lemma 5.7. (Trace inequality) For any $v \in H^L(K)$, we have the following revised form of trace inequality

$$|v_x(x_{j+\frac{1}{2}})|^2 \leq C(\alpha,\beta)(h^{-1}|v|^2_{1,I_j} + h|v|^2_{L,I_j}). \tag{5.34}$$

Proof. If $w \in H^2(K)$, we have the following trace inequality (see Thm 3.10 in [7])

$$\left\| \frac{\partial w}{\partial n} \right\|^2_{0,\partial K} \leq C(h^{-1}|w|^2_{1,K} + h|w|^2_{2,K}), \tag{5.35}$$

where e is an edge of K and C depends only on the minimum angle of K.

Applying the same change of variables (5.29),

$$\begin{aligned}
|v_x(x_{j+\frac{1}{2}})|^2 &= |\tfrac{1}{a^\varepsilon} \tilde{v}_{\tilde{x}}(\tilde{x}_{j+\frac{1}{2}})|^2 \\
&\leq C(\tilde{h}^{-1}|\tilde{v}|^2_{1,\tilde{I}_j} + \tilde{h}|\tilde{v}|^2_{2,\tilde{I}_j}) \\
&\leq C(h^{-1}\textstyle\int_{\tilde{I}_j} |\tilde{v}_{\tilde{x}}|^2 d\tilde{x} + h \int_{\tilde{I}_j} |\tilde{v}_{\tilde{x}\tilde{x}}|^2 d\tilde{x}) \\
&\leq C(h^{-1}\textstyle\int_{I_j} a^\varepsilon |v_x|^2 dx + h \int_{I_j} a^\varepsilon |(a^\varepsilon v_x)_x|^2 dx) \\
&\leq C(\alpha,\beta)(h^{-1}|v|^2_{1,I_j} + h|v|^2_{L,I_j}).
\end{aligned} \tag{5.36}$$

□

Lemma 5.8. (Error Estimates) Let $u(x)$ be the exact solution of (5.3) and u_h be the numerical solution computed by the multiscale Babuška-Zlámal method. There

exists some constant C independent of ε such that

$$\|u - u_h\|_{0,\Omega} \leq Ch^{k+1}\|f\|_{k-1,\Omega}. \tag{5.37}$$

Proof. We begin with an estimate which will be useful in what follows. For any $v, w \in V(h)$,

$$\begin{aligned} &\textstyle\sum_{j=1}^{N} a^{\varepsilon}\{v_x\}_{j+\frac{1}{2}}[w]_{j+\frac{1}{2}} = \sum_{j=1}^{N} h^{(k+\frac{1}{2})}\{a^{\varepsilon}v_x\}_{j+\frac{1}{2}} h^{-(k+\frac{1}{2})}[w]_{j+\frac{1}{2}} \\ &\leq C \,|||\, w \,|||\, \left(\textstyle\sum_{j=1}^{N} h^{2k+1}\{a^{\varepsilon}v_x\}^2_{j+\frac{1}{2}}\right)^{\frac{1}{2}} \leq Ch^k \,|||\, w \,|||\, \|v\|_{L,h} \ , \end{aligned} \tag{5.38}$$

where $\{u\} = \frac{1}{2}(u^+ + u^-)$. The last inequality comes from the Lemma 5.7. The Babuška-Zlámal DG method is not consistent, instead of satisfying the consistency condition, it satisfies

$$B_h(u, v) = \int_0^1 fv dx + \sum_{j=0}^{N} a^{\varepsilon}\{u_x\}_{j+\frac{1}{2}}[v]_{j+\frac{1}{2}}, \quad \forall v|_K \in H^1(I_j). \tag{5.39}$$

It is neither adjoint consistent. We have

$$B_h(v, \varphi) = \int_0^1 vg dx + \sum_{j=0}^{N} a^{\varepsilon}\{\varphi_x\}_{j+\frac{1}{2}}[v]_{j+\frac{1}{2}}, \quad \forall v|_K \in H^1(I_j), \tag{5.40}$$

where φ is the exact solution of the adjoint problem of (5.3) , which is

$$-(a^{\varepsilon}(x)\varphi_x)_x = g(x), \quad 0 \leq x \leq 1, \tag{5.41}$$

with the boundary condition

$$\varphi(0) = \varphi(1) = 0. \tag{5.42}$$

From the stability of the Babuška-Zlámal method, we obtain

$$C_s \,|||\, u_I - u_h \,|||^2 \leq B_h(u_I - u, u_I - u_h) + B_h(u - u_h, u_I - u_h) := T_1 + T_2. \tag{5.43}$$

Let u_I be the continuous interpolant (5.6) of u in S^k, using the approximation property (5.5), we have

$$T_1 \leq C_B \,|||\, u_I - u \,|||\, |||u_I - u_h||| \leq C_B C_i h^k \,|||\, u_I - u_h \,|||\, \|f\|_{k-1,\Omega}. \tag{5.44}$$

The term T_2 arises from the inconsistency of the method, it can be estimated by using our auxiliary inequality (5.38) and Lemma 5.6:

$$\begin{aligned} T_2 &= \textstyle\sum_{j=1}^{N} a^{\varepsilon}\{u_x\}_{j+\frac{1}{2}}[u_I - u_h]_{j+\frac{1}{2}} \\ &\leq Ch^k \,|||\, u_I - u_h \,|||\, \|u\|_{L,\Omega} \leq Ch^k \,|||\, u_I - u_h \,|||\, \|f\|_{0,\Omega}. \end{aligned} \tag{5.45}$$

Hence, inserting (5.44) and (5.45) into (5.43), we get

$$|||u_I - u_h||| \leq Ch^k \|f\|_{k-1,\Omega},$$

and the optimal order estimate

$$|||u - u_h||| \leq Ch^k \|f\|_{k-1,\Omega}. \tag{5.46}$$

For the L^2-error estimate, we have

$$\|u - u_h\|_{0,\Omega}^2 = B_h(u - u_h, \varphi) - \sum_{j=1}^{N} a^{\varepsilon}\{\varphi_x\}_{j+\frac{1}{2}}[u - u_h]_{j+\frac{1}{2}} =: T_3 + T_4. \tag{5.47}$$

Let φ_I be any continuous interpolant of φ in S^k, then $B_h(u, \varphi_I) = \int_0^1 f\varphi_I dx$. Therefore,

$$T_3 = B_h(u - u_h, \varphi - \varphi_I) \leq C_B \,|||u - u_h|||\, |||\varphi - \varphi_I||| \leq Ch \,|||u - u_h|||\, \|u - u_h\|_{0,\Omega}. \tag{5.48}$$

The term T_4 arises from the adjoint inconsistency and can be estimated by means of

the auxiliary inequality (5.38) as follows:

$$T_4 \leq Ch^k \,|||\, u - u_h \,|||\, \|\varphi\|_{L,\Omega} \leq Ch^k \,|||\, u - u_h \,|||\, \|u - u_h\|_{0,\Omega}, \tag{5.49}$$

where again we used elliptic regularity Lemma 5.6. Inserting (5.48) and (5.49) into (5.47) and using (5.46), we obtain the desired optimal estimate,

$$\|u - u_h\|_{0,\Omega} \leq Ch^{k+1}\|f\|_{k-1,\Omega}. \tag{5.50}$$

□

5.4 A 1-D numerical example

In this section, we consider the same example as in [75], but we will use the proposed multiscale LDPG method in Sec. 5.2.1. Comparing with the Babuška-Zlámal DG method, LDG method is a stable, consistent and conservative method and it has smaller condition number of the mass matrix (see [19]).

The numerical example we test on is the elliptic multiscale problem (5.3) with

$$a^\varepsilon(x) = \frac{1}{2 + x + \sin\left(\frac{2\pi x}{\varepsilon}\right)}, \quad f = x, \tag{5.51}$$

with $\varepsilon = 0.01$ and $\varepsilon = 0.001$ respectively. The numerical results are shown in Table 5.1. We can clearly see a $(k+1)$th order of accuracy of the results obtained by multiscale LDPG method. However, the MD-LDG method based on polynomial basis does not have the expected order of convergence until the mesh is refined enough relative to ε, which is consistent with the error estimates for such DG method based on regular piecewise polynomials.

We also list the numerical results using multiscale interior penalty (IP [8]) DG method with $\varepsilon = 0.1$ and $\varepsilon = 0.01$ in Table 5.2. IP method is also a stable, consistent

and conservative method with small condition number of the mass matrix. The multiscale IP-DG method is the IP method based on the multiscale approximation space S^k. We use a stabilization parameter $\eta = 10$ in our test. We can clearly see a $(k+1)$th order of accuracy.

Table 5.1: L^2 errors and orders of accuracy for the multiscale LDPG method: 1-D case.

	$\varepsilon = 0.01$				$\varepsilon = 0.001$			
	S^1 space		P^1 space		S^1 space		P^1 space	
N	L^2 error	Order	L^2 error	Order	L^2 error	Order	L^2 error	Order
10	9.10E-4	–	9.87E-3	–	9.23E-4	–	1.02E-2	–
20	2.32E-4	1.97	9.74E-3	0.02	2.38E-4	1.95	1.00E-2	0.03
40	6.03E-5	1.94	9.72E-3	0.00	5.99E-5	1.99	9.97E-3	0.00
80	1.51E-5	2.00	1.07E-2	-0.14	1.51E-5	1.99	1.00E-2	-0.01
160	3.70E-6	2.03	3.80E-3	1.49	3.78E-6	2.00	1.03E-2	-0.03
320	9.54E-7	1.95	3.72E-4	3.35	9.47E-7	2.00	1.04E-2	-0.02
640	2.42E-7	1.98	2.80E-5	3.73	2.40E-7	1.98	8.87E-3	0.23
1280	6.08E-8	1.99	3.01E-6	3.21	5.77E-8	2.05	6.71E-3	0.40
2560	1.52E-8	2.00	6.29E-7	2.26	1.48E-8	1.96	8.25E-4	3.02
	S^2 space		P^2 space		S^2 space		P^2 space	
N	L^2 error	Order	L^2 error	Order	L^2 error	Order	L^2 error	Order
10	1.20E-5	–	9.98E-3	–	1.22E-5	–	1.03E-2	–
20	1.50E-6	3.00	9.80E-3	0.03	1.53E-6	3.00	1.01E-2	0.03
40	1.95E-7	2.95	9.99E-3	-0.03	1.90E-7	3.00	1.00E-2	0.00
80	2.34E-8	3.05	7.65E-3	0.39	2.40E-8	2.99	1.00E-2	0.00
160	2.92E-9	3.01	4.79E-4	4.00	3.00E-9	3.00	9.71E-3	0.04
320	3.79E-10	2.95	1.24E-5	5.28	3.76E-10	3.00	9.17E-3	0.08
640	4.83E-11	2.97	7.93E-7	3.96	4.55E-11	3.04	1.00E-2	-0.13
1280	6.12E-12	2.98	9.72E-8	3.02	5.73E-12	2.99	1.40E-3	2.84

Table 5.2: L^2 errors and orders of accuracy for the multiscale IP-DG method:1-D case.

	$\varepsilon = 0.1$				$\varepsilon = 0.01$			
	S^1 space		S^2 space		S^1 space		S^2 space	
N	L^2 error	Order	L^2 error	Order	L^2 error	Order	L^2 error	Order
10	9.19E-4	–	1.17E-5	–	1.03E-3	–	1.16E-5	–
20	2.63E-4	1.81	1.47E-6	2.99	2.61E-4	1.98	1.48E-6	2.97
40	6.78E-5	1.95	1.85E-7	2.99	6.71E-5	1.96	1.89E-7	2.97
80	1.73E-5	1.97	2.34E-8	2.98	1.68E-5	2.00	2.29E-8	3.04
160	4.33E-6	2.00	2.94E-9	2.99	3.89E-6	2.11	2.84E-4	3.01

5.5 The 2-D case

We now consider the 2-D elliptic multiscale problem

$$-(a^\varepsilon(x)u_x)_x - (b^\varepsilon(y)u_y)_y = f(x,y), \quad (x,y) \in \Omega, \tag{5.52}$$

with the boundary condition

$$u(x,y) = 0, \quad (x,y) \in \partial\Omega.$$

The 1-D approach can be easily expanded to the 2-D case, i.e. we construct the 2-D multiscale approximation space as follows:

$$S_2^k = \{\phi \in H^1(0,1) : -(a^\varepsilon(x)\phi_x)_x - (b^\varepsilon(y)\phi_y)_y|_K \in P^{k-2}(K)\}, \tag{5.53}$$

where K is a 2-D element with the barycenter at the point (x_K, y_K). Especially,

$$S_2^1 = \left\{ v : v|_K \in \text{span}\left\{1, \int_{x_K}^x \frac{1}{a^\varepsilon(\xi)}d\xi, \int_{y_K}^y \frac{1}{b^\varepsilon(\eta)}d\eta, \right\}\right\}, \tag{5.54}$$

and for S_2^2, we need to add

$$\left\{\int_{x_K}^{x}\frac{\xi-x_K}{a^\varepsilon(\xi)}d\xi,\int_{x_K}^{x}\frac{1}{a^\varepsilon(\xi)}d\xi\int_{y_K}^{y}\frac{1}{b^\varepsilon(\eta)}d\eta,\int_{y_K}^{y}\frac{\eta-y_K}{b^\varepsilon(\eta)}d\eta\right\}.$$

Unfortunately, for S_2^k with $k>2$, the basis functions may not be available explicitly and must be computed numerically.

Remark 5.2. The L^2 approximation property for S_2^1 is in [75]. However, the convergence proofs to 2-D case are not a trivial expansion of 1-D. The main difficulty is it is hard to find a continuous $u_I \in S^k$ for triangle or rectangle mesh.

5.5.1 A special 2-D example

Since it is difficult to find an analytical solution of (5.52), we are only able to test on a very special example. Consider problem (5.52) with

$$f=x+y,\quad a^\varepsilon(x)=\frac{1}{2+x+\sin\left(\frac{2\pi x}{\varepsilon}\right)},\quad b^\varepsilon(y)=\frac{1}{2+y+\sin\left(\frac{2\pi y}{\varepsilon}\right)},\tag{5.55}$$

for $x,y\in[0,1]^2$. The exact solution is $u_1(x)+u_1(y)$, where $u_1(x)$ is the exact solution to 1-D problem (5.3). Therefore, the boundary conditions are $u(x,0)=u_1(x)$, $u(0,y)=u_1(y)$, $u(x,1)=u_1(x)$ and $u(1,y)=u_1(y)$. Although the boundary conditions are not zero, the values at boundaries can be bounded by f (see Lemma 5.6).

We list the approximation results of S_2^k spaces in Table 5.3. We can see that S_2^k spaces have an optimal order of approximation rate, whereas the regular polynomial spaces p^k do not have it until the mesh is refined enough. The errors of accuracy obtained the multiscale IP-DG method are shown in Table 5.4. We can see the multiscale IP-DG method gives an optimal $(k+1)$th order of accuracy for the multiscale problem (5.55).

Table 5.3: L^2 errors and orders of S_2^k approximation to the solution of (5.55): 2-D case.

	$\varepsilon = 0.1$				$\varepsilon = 0.01$			
	S_2^1 space		P^1 space		S_2^1 space		P^1 space	
N	L^2 error	Order	L^2 error	Order	L^2 error	Order	L^2 error	Order
10	7.89E-4	–	2.07E-3	–	8.38E-4	–	9.06E-4	–
20	2.10E-4	1.91	3.61E-4	2.52	2.10E-4	1.99	3.21E-4	1.50
40	5.24E-5	2.00	2.18E-4	0.73	5.28E-5	2.00	2.45E-4	0.39
80	1.32E-5	1.99	5.61E-5	1.96	1.30E-5	2.02	2.29E-4	0.10
160	3.32E-6	2.00	1.41E-5	1.99	3.20E-6	2.02	1.10E-4	1.06
	S_2^2 space		P^2 space		S_2^2 space		P^2 space	
N	L^2 error	Order	L^2 error	Order	L^2 error	Order	L^2 error	Order
5	8.43E-5	–	2.30E-3	–	8.97E-5	–	3.45E-4	–
10	1.11E-5	2.93	6.57E-4	1.81	1.12E-5	3.00	2.41E-4	0.52
20	1.42E-6	2.96	2.86E-4	1.20	1.41E-6	2.99	2.38E-4	0.02
40	1.78E-7	2.99	2.86E-5	3.32	1.80E-7	2.97	2.38E-4	0.00
80	2.56E-8	2.98	3.65E-6	2.97	2.13E-8	3.07	1.71E-4	0.49
160	2.83E-9	2.99	4.59E-7	2.99	2.65E-9	3.01	3.78E-5	2.17

5.6 Concluding remarks

DG methods based on multiscale approximation spaces for solving a class of second order elliptic equations are presented in this chapter. We generalize and complete the proofs in [75] for the Babuška-Zlámal DG method in the case that the solution is not in H^2. We develop a multiscale LDPG method based on the multiscale approximation spaces. Both 1-D and special 2-D examples are presented. In future work, we will generalize the analysis to 2-D and other DG methods and we will test on more general 2-D examples.

Table 5.4: L^2 errors and orders of accuracy for the multiscale IP-DG method:2-D case.

	$\varepsilon = 0.1$				$\varepsilon = 0.01$			
	S_2^1 space		S_2^2 space		S_2^1 space		S_2^2 space	
N	L^2 error	Order	L^2 error	Order	L^2 error	Order	L^2 error	Order
5	4.35E-3	–	1.15E-4	–	4.44E-3	–	1.17E-4	–
10	1.07E-3	2.03	1.52E-5	2.91	1.17E-3	1.93	1.52E-5	2.94
20	3.07E-4	1.80	1.95E-6	2.96	3.01E-4	1.96	1.94E-6	2.97
40	7.98E-5	1.94	2.46E-7	2.99	7.85E-5	1.94	2.49E-7	2.96
80	2.04E-5	1.96	3.11E-8	2.98	1.99E-5	1.98	3.00E-8	3.05

Bibliography

[1] N. Ben Abdallah, P. Degond, and P.A. Markowich. On a one-dimensional schrödingerpoisson scattering model. *Z. Angew. Math. Phys.*, 48:135–155, 1997.

[2] N. Ben Abdallah, M. Mouis, and C. Negulescu. An accelerated algorithm for 2D simulations of the quantum ballistic transport in nanoscale MOSFETs. *J. Comput. Phys.*, 225:74–99, 2007.

[3] N. Ben Abdallah and O. Pinaud. Multiscale simulation of transport in an open quantum system: Resonances and wkb interpolation. *J. Comput. Phys.*, 213:288–310, 2006.

[4] N. Ben Abdallah, O. Pinaud, Carl L. Gardner, and C. Ringhofer. A comparison of resonant tunneling based on Schrödingers equation and quantum hydrodynamics. *VLSI Design*, 15:695–700, 2002.

[5] R. Abedi, B. Petracovici, and R.B. Haber. A space-time discontinuous Galerkin method for linearized elastodynamics with element-wise momentum balance. *Comput. Methods. Appl. Mech. Engrg.*, 195:3247–3273, 2006.

[6] F.F. Abraham, J.Q. Broughton, N. Bernstein, and E. Kaxiras. Spanning the continuum to quantum length scales in a dynamic simulation of brittle fracture. *Europhys. Lett*, 44:783–787, 1998.

[7] S. Agmon. *Lectures on elliptic boundary value problems.* Van Nostrand, Princeton, NJ, 1965.

[8] D. N. Arnold. An interior penalty finite element method with discontinuous elements. *SIAM J. Numer. Anal*, 39:742–760, 1982.

[9] D.N. Arnold, F. Brezzi, B. Cockburn, and L.D. Marini. Unified analysis of discontinuous Galerkin methods for elliptic problems. *SIAM J. Numer. Anal.*, 39:1749–1779, 2002.

[10] N. W. Ashcroft and N. D. Mermin. *Solid State Physics*. Brooks Cole, 1976.

[11] I. Babuška, G. Caloz, and J. Osborn. Special finite element methods for a class of second order elliptic problems wth rough coefficients. *SIAM J. Numer. Anal*, 31:945–981, 1994.

[12] I. Babuška and J. Osborn. Generalized finite element methods: Their performance and their relation to mixed methods. *SIAM J. Numer. Anal*, 20:510–536, 1983.

[13] I. Babuška and M. Zlámal. Nonconforming elements in the finite element method with penalty. *SIAM J. Numer. Anal*, 10:863–875, 1973.

[14] E. Bécache, S. Fauqueux, and P. Joly. Stability of perfectly matched layers, group velocities and anisotropic waves. *J. Comput. Phys.*, 188:399–433, 2003.

[15] J.P. Bérenger. A perfectly matched layer for the absorption of electromagnetic waves. *J. Comput. Phys.*, 114:185–200, 1994.

[16] D. Bohm. *Quantum Theory*. Dover, New York, 1989.

[17] D. Brown and S. Neyertz. A general pressure tensor calculation for molecular dynamics simulations. *Mol. Phys.*, 84:577–595, 1995.

[18] H.J. Castejon. Nonequilibrium molecular dynamics calculation of the thermal conductivity of solid materials. *J. Phys. Chem. B*, 107:826–828, 2003.

[19] P. Castillo. Performance of discontinuous Galerkin methods for elliptic PDEs. *SIAM J. Sci. Comput.*, 24:524–547, 2002.

[20] P. Castillo, B. Cockburn, I. Perugia, and D. Schötzau. An a priori error analysis of the local discontinuous Galerkin method for elliptic problems. *SIAM J. Numer. Anal*, 38:1676–1706, 2000.

[21] S. Chen, W. E, Y.-X. Liu, and C.-W. Shu. A discontinuous Galerkin implementation of a domain decomposition method for kinetic-hydrodynamic coupling multiscale problems in gas dynamics and device simulations. *J. Comput. Phys.*, 225:1314–1330, 2007.

[22] Z. Chen, B. Cockburn, C. Gardner, and J.W. Jerome. Quantum hydrodynamic simulation of hysteresis in the resonant tunneling diode. *J. Comput. Phys.*, 117:274–280, 1995.

[23] Z. Chen, B. Cockburn, J.W. Jerome, and C.-W. Shu. Mixed-RKDG finite element methods for the 2d hydrodynamic model for semiconductor device simulation. *VLSI Design*, 3:145–158, 1995.

[24] B. Cockburn. Discontinuous Galerkin methods for convection-dominated problems. In *High-Order Methods for Computational Physics, Lect. Notes Comput. Sci. Eng. 9, T. J. Barth and H.Deconinck, eds.*, pages 69–224. Springer, Berlin, 1999.

[25] B. Cockburn and B. Dong. An analysis of the minimal dissipation local discontinuous Galerkin method for convection-diffusion problems. *J. Sci. Comput.*, 32:233–262, 2007.

[26] B. Cockburn, S. Hou, and C.-W. Shu. The Runge-Kutta local projection discontinuous Galerkin finite element method for conservation laws IV: The multidimensional case. *Math. Comp.*, 54:545–581, 1990.

[27] B. Cockburn, G. Kanschat, I. Perugia, and D. Schötzau. Superconvergence of the local discontinuous Galerkin method for elliptic problems on cartesian grids. *SIAM J. Numer. Anal*, 39:264–285, 2001.

[28] B. Cockburn, F. Li, and C.-W. Shu. Locally divergence-free discontinuous Galerkin methods for the Maxwell equations. *J. Comput. Phys.*, 194:588–610, 2004.

[29] B. Cockburn, S.-Y. Lin, and C.-W. Shu. TVB Runge-Kutta local projection discontinuous Galerkin finite element method for conservation laws III: One dimensional systems. *J. Comput. Phys.*, 84:90–113, 1989.

[30] B. Cockburn and C.-W. Shu. TVB Runge-Kutta local projection discontinuous Galerkin finite element method for conservation laws II: General framework. *Math. Comp.*, 52:411–435, 1989.

[31] B. Cockburn and C.-W. Shu. The local discontinuous Galerkin method for time-dependent convection-diffusion systems. *SIAM J. Numer. Anal.*, 35:2440–2463, 1998.

[32] B. Cockburn and C.-W. Shu. TVB Runge-Kutta local projection discontinuous Galerkin finite element method for conservation laws V: multidimensional systems. *J. Comput. Phys.*, 141:199–224, 1998.

[33] B. Cockburn and C.-W. Shu. Runge-Kutta discontinuous Galerkin methods for convection-dominated problems. *J. Sci. Comput.*, 16:173–261, 2001.

[34] F. Collino and C. Tsogka. Application of the PML absorbing layer model to the linear elastodynamic problem in anisotropic heterogeneous media. *Geophysics*, 66:294–307, 2001.

[35] F. Costanzo and H. Huang. Proof of unconditional stability for a single-field discontinuous Galerkin finite element formulation for linear elasto-dynamics. *Comput. Methods. Appl. Mech. Engrg.*, 194:2059–2076, 2005.

[36] C. M. Dafermos. *Hyperbolic Conservation Laws in Continuum Physics.* Springer, second edition, 2005.

[37] M.S. Daw and M.I. Baskes. Embedded-atom method: derivation and application to impurities, surfaces, and other defects in metals. *Phys. Rev. B*, 29:6443–6453, 1984.

[38] M. Dumbser and M. Käser. An arbitrary high-order discontinuous Galerkin method for elastic waves on unstructured meshes - II. The three-dimensional isotropic case. *Geophys. J. Int*, 167:319–336, 2006.

[39] W. E and B. Engquist. The heterogeneous multi-scale methods. *Comm. Math. Sci.*, 1:87–132, 2003.

[40] W. E, B. Engquist, X. Li, W. Ren, and E. Vanden-Eijnden. Heterogeneous multiscale method: A review. *Commun. Comput. Phys.*, 2:367–450, 2007.

[41] D. Frenkel and B. Smit. *Understanding Molecular Simulation: from Algorithms to Applications.* Academic Press, second edition, 2002.

[42] H. K. Gummel. A self-consistent iterative scheme for one-dimensional steady state transistor calculations. *IEEE Trans. Electron Devices*, 11:455–465, 1964.

[43] W.G. Hoover. Canonical dynamics: Equilibrium phase-space distributions. *Phys. Rev. A(3)*, 31:1695–1697, 1985.

[44] H. Huang and F. Costanzo. On the use of space-time finite elements in the solution of elasto-dynamic problems with strain discontinuities. *Comput. Methods. Appl. Mech. Engrg.*, 191:5315–5343, 2002.

[45] T.J.R. Hughes and G.M. Hulbert. Space-time finite element methods for elastodynamics: formulations and error estimates. *Comput. Methods. Appl. Mech. Engrg.*, 66:339–363, 1988.

[46] J.H. Irving and J.G. Kirkwood. The statistical mechanical theory of transport processes IV. *J. Chem. Phys.*, 18:817–829, 1950.

[47] M. Käser and M. Dumbser. An arbitrary high-order discontinuous Galerkin method for elastic waves on unstructured meshes - I. The two-dimensional isotropic case with external source terms. *Geophys. J. Int*, 166:855–877, 2006.

[48] D.K. Khalmanova and F. Costanzo. A space-time discontinuous Galerkin finite element method for fully coupled linear thermo-elasto-dynamic problems with strain and heat flux discontinuities. *Comput. Methods. Appl. Mech. Engrg.*, 197:1323–1342, 2008.

[49] J. Knap and M. Ortiz. An analysis of the quasicontinuum method. *J. Mech. Phys. Solids*, 49:1899–1923, 2001.

[50] L.D. Landau and E. M. Lifshitz. *Theory of Elasticity.* Elsevier Science Ltd, 1986.

[51] R. J. LeVeque. *Numerical Methods for Conservation Laws.* Birkhäuser Basel, 1990.

[52] F. Li and C.-W. Shu. Reinterpretation and simplified implementation of a discontinuous Galerkin method for Hamilton-Jacobi equations. *App. Math. Lett.*, 18:1204–1209, 2005.

[53] X. Li and W. E. Multiscale modeling for dynamics of solids at finite temperature. *J. Mech. Phys. Solids*, 53:1650–1685, 2005.

[54] X. Li and W. E. Variational boundary conditions for molecular dynamics simulations of solids at low temperature. *Commun. Comput. Phys.*, 1:135–175, 2006.

[55] X. Li and W. E. Boundary conditions for molecular dynamics simulations of solids: Treatment of the heat bath. *Phys. Rev. B(3)*, 76:104107, 2007.

[56] Y. Liu and C.-W. Shu. Local discontinuous Galerkin methods for moment models in device simulations: Formulation and one-dimensional results. *J. Comput. Electron.*, 3:263–267, 2004.

[57] Y. Liu and C.-W. Shu. Local discontinuous Galerkin methods for moment models in device simulations: Performance assessment and two-dimensional results. *Appl. Num. Math.*, 57:629–645, 2007.

[58] C. Negulescu. Numerical analysis of a multiscale finite element scheme for the resolution of the stationary Schrödinger equation. *Numer. Math.*, 108:625–652, 2008.

[59] C. Negulescu, N. Ben Abdallah, E. Polizzi, and M. Mouis. Simulation schemes in 2D nanoscale MOSFETs: A WKB based method. *J. Comput. Electron.*, 3:397–400, 2004.

[60] H. Nessyahu and E. Tadmor. Nonoscillatory central differencing for hyperbolic conservation laws. *J. Comput. Phys.*, 87:408–463, 1990.

[61] S. Nosé. A unified formulation of the constant temperature molecular dynamics method. *J. Chem. Phys.*, 81:511–519, 1984.

[62] R. E. Peierls. *Quantum Theory of Solids.* Oxford University Press, UK, 1956.

[63] O. Pinaud. Transient simulations of a resonant tunneling diode. *J. Appl. Phys.*, 92:1987–1994, 2002.

[64] E. Polizzi and N. Ben Abdallah. Subband decomposition approach for the simulation of quantum electron transport in nanostructures. *J. Comput. Phys.*, 202:150–180, 2005.

[65] B. Rivière, S. Shaw, M.F. Wheeler, and J.R. Whiteman. Discontinuous Galerkin finite element methods for linear elasticity and quasistatic linear viscoelasticity. *Numer. Math.*, 95:347–376, 2003.

[66] C.-W. Shu. TVB uniformly high-order schemes for conservation laws. *Math. Comp.*, 49:105–121, 1987.

[67] C.-W. Shu and S. Osher. Efficient implementation of essentially non-oscillatory shock-capturing schemes. *J. Comput. Phys.*, 77:439–471, 1988.

[68] E.B. Tadmor, M. Ortiz, and R. Phillips. Quasicontinuum analysis of defects in crystals. *Philos. Mag. A*, 73:1529–1564, 1996.

[69] S. Tang, T.Y. Hou, and W.K. Liu. A pseudo-spectral multiscale method: interfacial conditions and coarse grid equations. *J. Comput. Phys.*, 213:57–85, 2006.

[70] J. Tersoff. New empirical model for the structural properties of silicon. *Phys. Rev. Lett.*, 56:632–635, 1986.

[71] G.J. Wagner and W.K. Liu. Coupling of atomistic and continuum simulations using a bridging scale decomposition. *J. Comput. Phys.*, 190:249–274, 2003.

[72] S.P. Xiao and T. Belytschko. A bridging domain method for coupling continua with molecular dynamics. *Comput. Methods. Appl. Mech. Engrg.*, 193:1645–1669, 2004.

[73] J. Yan and C.-W. Shu. A local discontinuous Galerkin method for KdV type equations. *SIAM J. Numer. Anal.*, 40:769–791, 2002.

[74] L. Yuan and C.-W. Shu. Discontinuous Galerkin method based on non-polynomial approximation spaces. *J. Comput. Phys.*, 218:295–323, 2006.

[75] L. Yuan and C.-W. Shu. Discontinuous Galerkin method for a class of elliptic multi-scale problems. *Int. J. Numer. Meth. Fluids*, 56:1017–1032, 2008.